



Chinese Pharmaceutical Association
Institute of Materia Medica, Chinese Academy of Medical Sciences

Acta Pharmaceutica Sinica B

www.elsevier.com/locate/apsb
www.sciencedirect.com



ORIGINAL ARTICLE

Photosensitive pro-drug nanoassemblies harboring a chemotherapeutic dormancy function potentiates cancer immunotherapy



Jianjun Cheng^{a,c,f,1}, Haitian Zhao^{a,d,e,1}, Bin Li^{b,1}, Hua Zhang^c,
Qianyu Zhao^{a,c}, Shiyao Fu^{a,c}, Ying Han^{a,c}, Weihong Lu^{a,d,e},
Jiahua Shi^f, Xin Yang^{a,c,d,e,*}

^aSchool of Medicine and Health, Harbin Institute of Technology, Harbin 150001, China

^bAcademician Workstation, Jiangxi University of Chinese Medicine, Nanchang 330004, China

^cSchool of Chemistry and Chemical Engineering, Harbin Institute of Technology, Harbin 150001, China

^dChongqing Research Institute, Harbin Institute of Technology, Chongqing 401135, China

^eNational and Local Joint Engineering Laboratory for Synthesis, Transformation and Separation of Extreme Environmental Nutrients, Harbin 150001, China

^fKey Laboratory of Natural Medicine and Immune-Engineering of Henan Province, Henan University, Kaifeng 475004, China

Received 11 February 2022; received in revised form 28 April 2022; accepted 10 May 2022

KEY WORDS

Cancer immunotherapy;
Nano-immunostimulants;
Chemotherapeutic
dormancy;
Pro-drug;
Self-assembly;
Natural small molecule;
Betulinic acid;
Photodynamic therapy

Abstract Immunotherapy combined with effective therapeutics such as chemotherapy and photodynamic therapy have been shown to be a successful strategy to activate anti-tumor immune responses for improved anticancer treatment. However, developing multifunctional biodegradable, biocompatible, low-toxic but highly efficient, and clinically available transformed nano-immunostimulants remains a challenge and is in great demand. Herein, we report and design of a novel carrier-free photo-chemotherapeutic nano-prodrug COS-BA/Ce6 NPs by combining three multifunctional components—a self-assembled natural small molecule betulinic acid (BA), a water-soluble chitosan oligosaccharide (COS), and a low toxic photosensitizer chlorin e6 (Ce6)—to augment the antitumor efficacy of the immune adjuvant anti-PD-L1-mediated cancer immunotherapy. We show that the designed nanodrugs harbored a smart and distinctive “dormancy” characteristic in chemotherapeutic effect with desired lower cytotoxicity, and multiple favorable therapeutic features including improved ¹O₂ generation induced by

*Corresponding author. School of Medicine and Health, Harbin Institute of Technology, Harbin 150001, China.

E-mail address: yangxin@hit.edu.cn (Xin Yang).

Peer review under responsibility of Chinese Pharmaceutical Association and Institute of Materia Medica, Chinese Academy of Medical Sciences.

¹These authors made equal contributions to this work.

the reduced energy gap of Ce6, pH-responsiveness, good biodegradability, and biocompatibility, ensuring a highly efficient, synergistic photochemotherapy. Moreover, when combined with anti-PD-L1 therapy, both nano-coassembly based chemotherapy and chemotherapy/photodynamic therapy (PDT) could effectively activate antitumor immunity when treating primary or distant tumors, opening up potentially attractive possibilities for clinical immunotherapy.

© 2023 Chinese Pharmaceutical Association and Institute of Materia Medica, Chinese Academy of Medical Sciences. Production and hosting by Elsevier B.V. This is an open access article under the CC BY-NC-ND license (<http://creativecommons.org/licenses/by-nc-nd/4.0/>).

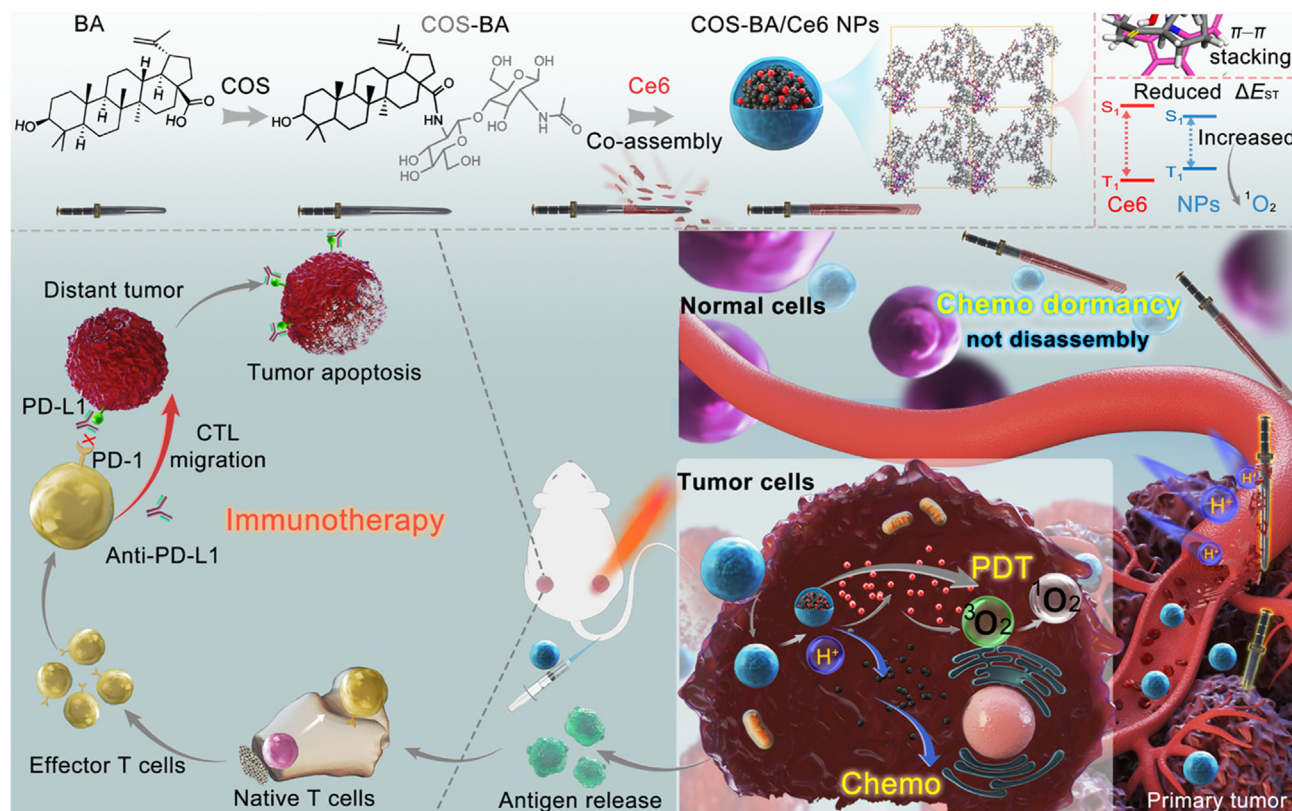
1. Introduction

Cancer immunotherapy, such as the immune checkpoint blockade strategy using PD-L1 or CTLA-4 to combat cancer by activating the host's own immune system, has undoubtedly revolutionized cancer treatment^{1,2}. Unfortunately, the weak immune response and ineffective therapeutic effects greatly limited its clinical prospects^{3,4}. Recently, current studies have revealed that a combination of immunotherapy with other modalities such as chemotherapy⁵, photodynamic therapy (PDT)⁶, photothermal therapy (PTT)⁷, and radiotherapy⁸, can effectively trigger antitumor immunogenicity by inducing cancer cells to undergo immunogenic cell death (ICD)⁹, which suggests the potential of immune modulation to activate anti-tumor immune responses. Numerous innovative designs of nanomaterials based on these synergistic combinations of immunotherapy strategies have achieved significantly improved anti-cancer activity including inorganic¹⁰, polymer¹¹, and biomimetic¹² nanoparticles (NPs). However, developing multifunctional biodegradable, biocompatible, low toxicity but highly efficient, and clinically available transformed nano-immunostimulants remains a great challenge and huge demand.

Natural biological materials like nucleic acids¹³, proteins¹², peptides^{14,15}, and small molecular natural products^{16,17} due to their inherent benefits (*e.g.*, biocompatibility, non-toxicity) have drawn a significant research interest for medical applications. Especially in recent years, anticancer bioactive terpenoid natural small molecules (NSMs) possessing a self-assembly function have been discovered successively^{18,19}. For example, betulinic acid (BA), ergosterol (ET), and abiatic acid (AA) can self-assemble into micron or nano-structured particles. These NSMs are attractive building blocks to use to develop antitumor agents for synergistic chemotherapy and PDT. They have been proven to exhibit significant benefits of easy nano-fabrication, better biocompatibility and biodegradability, lower toxicity with reduced liver injury, and high synergism in antitumor therapy^{20–23}. This provides promising alternatives for developing clinically available translatable nano-immunostimulants for synergistic immunotherapy. However, the generally stronger lipophilicity of these NSMs led to inefficient cellular endocytosis, which weakened their anticancer activity and limited their clinical value for cancer treatment²⁴. Similar to the commonly reported nanocomposites, the corresponding NSMs nano-formulations promoted cellular uptake to enhance chemotherapeutic effects, but also inadvertently increased the risk of nonspecific cytotoxicity to normal cells²². Therefore, how to maximize the anticancer efficacy of terpenoid NSMs nano-agents while minimizing its toxicity to normal tissue is worth thinking deeply as a crucial issue in synergistic immunotherapy process.

Pro-drug strategies have been extensively applied to improve the cell uptake of lipophilic small molecules by increasing hydrophilicity²⁵. Generally, amphiphilic drugs particularly possess higher cellular uptake efficiency than hydrophilic or lipophilic drugs²⁶. The higher the cellular phagocytosis, the better the therapeutic efficacy²⁴. Thus, developing amphiphilic terpenoid NSMs pro-drug molecules may be a potential method for maximizing their therapeutic effects. In addition, stimuli-responsive nanodrugs to the specific tumor microenvironment (*e.g.*, acid, redox responsiveness) hold great promise for controlling drug release, which is advantageous in suppressing the cytotoxicity of the chemotherapeutic drugs^{27,28}. Meanwhile, supramolecular co-assembly (*e.g.*, a reprecipitation approach) was an effective strategy to prepare highly water-soluble carrier-free nanodrugs^{22,29}, which might be expected to slightly decrease the phagocytosis efficiency of amphiphilic NSMs to some degree, thereby attenuating their pre-designed cytotoxicity. We hypothesize that stimuli-responsive and fully hydrophilic nanodrugs were further established based on amphiphilic NSMs pro-drug and can effectively suppress its nonspecific cytotoxicity to normal cells while stimulating the release of highly toxic amphiphilic NSMs into tumor cells, facilitating their dormancy in normal tissues and activation in tumor site. It is important to select the appropriate water-soluble and stimuli-responsive precursor to modify terpenoid NSMs to prepare amphiphilic pro-drug molecules. For years, chitosan oligosaccharides (COS), as the degraded products of chitosan, not only have good water solubility and abundant $-OH$ or $-NH_2$ groups that lead to a good pH response, but also have beneficial antitumor activities by enhancing the host's immune function through regulating the activity of immune cells such as monocyte macrophages and lymphocytes^{30,31}. These guarantee the huge possibility to construct stimuli-responsive target nano-immunostimulants for synergistic immunotherapy.

Herein, based on the above considerations, in our experimental design, a pentacyclic triterpene NSMs of betulinic acid (BA) is used as a potent anticancer agent³², COS was introduced to synthesize an amphiphilic COS-BA molecule to improve the chemotherapeutic effect. Chlorin e6 (Ce6), a widely utilized photosensitizer with very low/no dark toxicity³³, was employed to construct a completely water-soluble carrier-free photosensitive prodrug COS-BA/Ce6 NPs using a direct co-assembly strategy. COS-BA/Ce6 NPs combined two therapeutic modalities, chemotherapy and photodynamic therapy (PDT), which can effectively increase the presentation of tumor-derived antigens to T cells, generating robust immunological responses with the assistance of an immune adjuvant anti-PD-L1 to cause highly efficient and synergistic anti-tumor chemotherapy/PDT/immunotherapy (Scheme 1). The engineered COS-BA/Ce6 NPs showed a smart dormancy function with insidious chemotherapy effects, *i.e.*, non-



Scheme 1 PDT and chemotherapy of co-assembled COS-BA/Ce6 NPs potentiated anti-PD-L1 to induce a systemic antitumor immunotherapy. The introduction of water-soluble COS can effectively enhance the chemotherapeutic activity of BA (depicted as a half-sword), resulting in a hyperactive COS-BA amphiphilic prodrug (long-sword). When co-assembled with photosensitizer Ce6 (scabbard), the shell-structured and pH-sensitive nano-coassemblies had a smart and distinctive “dormancy” function with inhibited chemotherapeutic toxicity to normal tissues. But, once it arrived and was stimulated by the acidic (H^+) tumor microenvironment, the highly active amphiphilic prodrug COS-BA will be released resulting in significant chemotherapy. In addition, the constructed co-assemblies exhibited excellent PDT activity with enhanced singlet oxygen (1O_2) generation induced by the reduced energy gap between the singlet and triplet excited states (ΔE_{ST}) of Ce6. Combined with an anti-PD-L1 checkpoint blockade, the release of tumor-associated antigens after chemotherapy/PDT treatment can effectively activate a systemic antitumor immune response for distant cancer immunotherapy.

irradiated co-assembled NPs showed remarkably inhibited *in vitro* cytotoxicity compared to amphiphilic COS-BA whether against cancer or normal cells. Attributing to the distinctive pH-responsive behavior, it performs low-toxicity and biosafety to normal tissue *in vivo*, but is highly toxic to tumor tissue due to the stimulating release of hyperactive COS-BA in the weakly acidic tumor microenvironment³⁴. To our best knowledge, currently the designed nanodrugs harboring this chemotherapeutic dormancy function are still rarely reported. Meanwhile, the nanodrug has multiple favorable therapeutic features such as improved 1O_2 generation by reducing the energy gap (ΔE_{ST}) of Ce6, rapid biological metabolism, and enhanced tumor accumulation, which led to an efficient and safe antitumor combination of chemotherapy and PDT treatment. More importantly, both NPs-based chemotherapy and chemotherapy/PDT systems could effectively activate antitumor immunity by facilitating the proliferation of TNF- α and IFN- γ -producing CD8⁺ T cells in primary or distant tumors. Our proposed biodegradable, biocompatible, uniquely dormant, bio-safe, and highly efficient photo-chemotherapeutic nano-drug achieve significantly systemic immune therapeutic responses, opening up attractive possibilities for clinical application in treating distant or metastatic cancer therapy.

2. Materials and methods

2.1. Synthesis of COS-BA

Betulinic acid (40 mg, 0.1 mmol), EDC (38 mg, 0.2 mmol) and NHS (17 mg, 0.15 mmol) were dissolved in 3 mL of *N,N*-dimethylformamide (DMF). After stirred at room temperature for 30 min, 96 mg of COS water solution (1 mL) was gently added dropwise into the mixture and stirred for 24 h. Then the reaction mixture was diluted with CH_2Cl_2 , and extracted repeatedly. The CH_2Cl_2 layer was evaporated and purified on a silica gel column. The unreacted BA was removed initially using petroleum ether: acetone (5:1, *v/v*) as eluent, and then changed to 3:1 to yield white COS-BA (yield: 42%), where COS was identified as dimer ($n = 2$). 1H NMR (400 MHz, $CDCl_3$) δ : 8.98 (1H, s, BA-28 O=C-NH), 4.73 (1H, s, H-29a), 4.60 (1H, s, H-29b), 3.18 (1H, dd, $J = 4.8, 10.8$ Hz, H-3), 2.95–3.93 (8H, m, COS), 2.64 (3H, s, CH_3 -COS), 0.76 (3H, s, H-24), 0.83 (3H, s, H-25), 0.90 (3H, s, H-23), 0.97 (3H, s, H-26), 0.98 (3H, s, H-27), 1.70 (3H, s, H-30). ^{13}C NMR (100 MHz, $CDCl_3$) δ : 179.18 (CO, COS), 156.43 (C-28), 150.97 (C-20), 109.03 (C-29), 78.74, 77.04, 69.32, 69.22, 65.25, 58.14, 55.62, 55.21, 53.65, 53.22, 50.52, 45.96, 44.32,

44.11, 41.85, 40.59, 38.68, 38.55, 37.32, 37.04, 36.39, 35.31, 34.21, 31.81, 31.54, 31.17, 30.28, 29.09, 27.80, 27.22, 25.74, 25.53, 20.91, 19.48, 18.12, 16.02, 15.87, 15.17, 14.65, 14.62. ESI-MS m/z : 814.5871 $[M-6H]^-$ ($C_{44}H_{72}N_2O_{12}$).

2.2. Preparation of COS-BA/Ce6 NPs

Co-assembled COS-BA/Ce6 NPs were prepared by one step reprecipitation method. Typically, 5 μ L of Ce6 (33 mmol/L) and 40 μ L of COS-BA (33 mmol/L) DMSO solutions were first mixed. Subsequently, the mixture was injected rapidly into 1 mL of water containing 10 μ L of NaOH (50 mmol/L) under ultrasonication (KQ-250E, ShuMei, KunShan, China). After sonication for 10 min, the COS-BA/Ce6 NPs were obtained by centrifugation at 13,000 rpm (TGL-16G, Xiangyi, Changsha, China) for 25 min. Other formulations with different ratios of COS-BA to Ce6 were prepared by the same procedure with a constant NaOH to Ce6 molar ratio of 3:1.

2.3. Cell lines

Human MCF-7, HepG2, LO2, and mouse 4T1, L929 cell lines are provided by the Institute of Biochemistry and Cell Biology, SIBS, CAS (China). MCF-7, HepG2, LO2 were cultured in DMEM medium with 10% fetal bovine serum (FBS, Gibco) and 1% penicillin-streptomycin antibiotic (Life Technology, USA) at 37 °C. 4T1 and L929 were cultured in RMPI-1640 medium with the same ratio as above.

2.4. Cellular uptake and endocytic pathways studies

For investigation of cellular uptake, 4T1 or LO2 cells were incubated with free Ce6 or COS-BA/Ce6 NPs (equivalent concentration of Ce6: 1.7 μ g/mL, COS-BA: 19.5 μ g/mL, BA: 10.8 μ g/mL) for various times. After washing, fixing, and DIPA (#D9542, Sigma) staining, then the cells were imaged under a fluorescent inverted microscope (FIM) (DSY-2000X, UP Optotech, Changchun, China). The fluorescence intensity was determined using flow cytometry using the Guava EasyCyte mini system (Merck Millipore, Germany).

For quantification of the uptake efficiency, the cellular accumulation of BA and COS-BA was measured using HPLC (Agilent 1200, USA). Typically, 4T1 cells were treated with free COS-BA or BA (equivalent BA: 25 μ g/mL) for 0.5 and 3 h. After washing with PBS, the cell pellets were harvested and underwent ultrasonic homogenization (JY92-IIN, Scientz Biotechnology, Ningbo, China) for cell lysis. Then, COS-BA or BA was extracted by chloroform for HPLC analysis after lyophilizing the samples. The mobile phase was water (0.2% phosphoric acid) and acetonitrile at a flow rate of 1.0 mL/min, and corresponding volume ratios were 60:40 and 15:85 (v/v) for analysis of COS-BA and BA, respectively. The detection wavelength was 213 nm.

For investigation of endocytic pathways of COS-BA/Ce6 NPs, 4T1 cells were seeded in 6-well plates and incubated for 24 h before being pretreated with various endocytosis inhibitor for 30 min, including a micropinocytosis inhibitor [50 μ mol/L, ethylisopropyl amiloride (EIPA) (#N132356, Aladdin)], a clathrin-mediated endocytosis inhibitor [20 μ mol/L, chlorpromazine (#C7010, Solarbio)], a caveolae-mediated endocytosis inhibitor [25 μ mol/L, nystatin (#N0260, Solarbio)], and a lysosome acidification inhibitor [50 μ mol/L, chloroquine phosphate (#C9720, Solarbio)]³⁵. Next, the cells were further cultured with 2 mL of

COS-BA/Ce6 NPs (Ce6: 1.7 μ g/mL, COS-BA: 19.5 μ g/mL) for 2 h and imaged under FIM (UP Optotech). Where the cells incubated without endocytic inhibitor at 37 °C were set as control and at low-temperature incubation (4 °C) for evaluation of the energy-dependent endocytosis. Meanwhile, the mean fluorescence intensity of cells was also determined by flow cytometry.

2.5. Cytotoxicity assay

4T1 cells were seeded in a 96-well plate. Then the cells were treated with various concentrations of COS-BA NPs for 24 h. Afterward, 10 μ L of MTT (#M158055, Aladdin) dye (5 mg/mL) was added to the well and incubated for an additional 4 h, and then 150 μ L of DMSO was added to dissolve the formazan crystals. The absorbance of each well at 492 nm was recorded by a microplate reader. For the irradiation group, the cells were treated with drugs for 4 h, then irradiated for 10 min by 675 ± 10 nm light and incubated for an additional 20 h. The cytotoxicity of COS-BA/Ce6 NPs (1 μ g/mL of Ce6 corresponds to 11.5 μ g/mL COS-BA and 6.4 μ g/mL BA) against other cells (MCF-7, HepG2, LO2, and L929) were also determined by the same MTT assay only with a different medium. Meanwhile, the combination index was calculated by software CompuSyn 2.0 using Chou-Talalay theorem calculation³⁶.

2.6. Animal models

All experimental procedures were executed according to the protocols approved by Harbin Medical University Animal Care and Use Committee. 4T1 cells were suspended in RMPI-1640 medium and subcutaneously injected to the right-back of each female BALB/c mouse (18–22 g, 6–7 weeks old).

2.7. In/ex vivo fluorescence imaging

A 200 μ L of COS-BA/Ce6 NPs 5% glucose solution (equivalent Ce6: 0.35 mg/mL, COS-BA: 4.02 mg/mL) were injected through the tail vein into tumor-bearing mice. After that, fluorescence imaging of tumor sites at a predetermined time was performed using AniView 100/600 multi-model *in vivo* animal imaging system (Guangzhou Biolight Biotechnology Co., Ltd., China) with the excitation at 630 nm. After 24 h post-injection, the major organs (heart, liver, spleen, lung, and kidney) and tumor were collected for *ex vivo* fluorescence imaging. Besides, the *ex vivo* fluorescence images of tumors and major organs at different times after *i.v.* injections of Ce6 or COS-BA/Ce6 NPs were also evaluated.

2.8. In vivo chemotherapy/PDT

4T1-bearing mice (75–100 mm³) are randomly divided into six groups ($n = 5$): 1) 5% glucose solution; 2) Ce6; 3) Ce6 with irradiation; 4) COS-BA (40.2 mg/kg, where BA: 22.3 mg/kg); 5) COS-BA/Ce6 NPs; 6) COS-BA/Ce6 NPs with irradiation. For each group, mice are injected with 200 μ L of COS-BA/Ce6 NPs (equivalent Ce6: 3.5 mg/kg of body) through the tail vein on Days 0, 2 and 4. For the irradiation groups, at 4 h post-injection after each administration, all mice were anesthetized with isoflurane, and the tumor sites were irradiated by 675 ± 10 nm (150 mW/cm²) light for 15 min. Tumor volumes and body weights of mice are recorded every other day as well. Tumor volumes are calculated by the formula: $V = \text{width}^2 \times \text{length}/2$. After 14 days of treatment, the tumors were

excised and weighted to calculate the tumor inhibition ratio (TIR) by the commonly used equation: $TIR = (1 - m_{\text{sample}}/m_{\text{control}}) \times 100\%$. Where m_{sample} and m_{control} were the average tumor weight of each treated group and 5% glucose aqueous solution group, respectively.

2.9. *In vivo* chemotherapy/PDT/immunotherapy

To demonstrate the potential of COS-BA/Ce6 NPs combined with immunotherapy, the bilateral tumor model was designed through subcutaneous injection of 4T1 cells into the left and right flanks. When the tumors approached 75–100 mm³, the mice were divided into five groups. (1) Control; (2) COS-BA/Ce6 NPs (COS-BA = 40.2 mg/kg, where BA = 22.3 mg/kg); (3) COS-BA/Ce6 NPs + light; (4) COS-BA/Ce6 NPs + anti-PD-L1; (5) COS-BA/Ce6 NPs + anti-PD-L1 + light. On Day 0, 200 μ L of 5% glucose solution (Group 1) or COS-BA/Ce6 NPs (Ce6 = 3.5 mg/kg) (Group 2, 3, 4, 5) were i.v. injected into mice. After 4 h post-injection, the right tumors of Group 3 and 4 were irradiated for 15 min. The mice were anesthetized with isoflurane and rolled on one side to avoid exposing the left tumors. Then anti-PD-L1 antibody (BioXcell, product number: BE0101, clone number: 10F.9G2) was i.v. injected into mice for Group 4 and 5 on Days 2, 4, and 6 (15 μ g per mouse per injection). The length and width of each tumor were monitored every other day. After 14 days of treatment, the blood serum of mice was collected to evaluate interferon-gamma (IFN- γ) (#KMC4021) and tumor necrosis factor (TNF- α) (#BMS607-3) using ELISA assay (eBioscience). The tumors were collected, dissociated, treated with red blood cell lysis buffer, and washed with PBS by centrifugation. Then, the cell suspension was stained with anti-CD3-FITC (#MA1-10187, clone 145-2C11, eBioscience) and anti-CD8a-PE (#12-0081-85, clone 53-6.7, eBioscience). Afterward, the cytotoxic T lymphocytes (CTL) infiltration in right and left tumors after different treatments was evaluated by flow cytometry.

3. Results and discussion

3.1. Synthesis, fabrication, and characterization of COS-BA/Ce6 NPs

In this study, we design a novel prodrug small molecule COS-BA based on water-soluble chitosan oligosaccharide (COS), which may elevate the chemotherapeutic activity of pentacyclic triterpene betulinic acid (BA) by improving the cell uptake through increasing hydrophilicity. The COS (degree of polymerization, DP: 2–6) employed here was prepared by our previously described method³⁰. Then, the COS-BA was synthesized *via* a dehydration condensation reaction. Combined with the principal component analysis of COS, the chemical structure of COS-BA was thought to be a disaccharide (DP:2) modified BA (Supporting Information Fig. S1), which was confirmed by ¹H NMR, ¹³C NMR, and ESI-MS (Supporting Information Figs. S2–S4). Analysis of the representative ¹H NMR showed the distinct proton signal of COS around 2.64–3.93 ppm and C=CH₂ peaks (4.60, 4.73 ppm) of BA, demonstrating the successful synthesis of COS-BA (Fig. 1A). For preparation of the co-assembled synergistic antitumor reagent COS-BA/Ce6 NPs, a versatile re-precipitation approach was employed by cooperating with a highly efficient photosensitizer Ce6. By changing the initial molar ratios, both COS-BA/Ce6 co-assembly formulations could

form spherical nanostructures with modulated sizes (Fig. 1B and Supporting Information Fig. S5). Across different input ratios of COS-BA/Ce6, the hydrophilic diameters of COS-BA/Ce6 NPs were near 200–300 nm with a negative ζ -potential. Considering that NPs prepared at a formulations of 8:1 showed a lower polydispersity index (PDI, 0.143) with a relatively smaller size (249 nm), a sufficient amount of chemotherapeutic agent COS-BA was also required for the combinatorial treatment. Therefore, we chose the formulations of COS-BA/Ce6 (8:1) for the following study.

Under this optimization, COS-BA/Ce6 NPs exhibited narrow size distributions (Fig. 1C) and good water-solubility, indicating its colloidal nature (Fig. 1D). To explore the reasons behind this successful co-assembly, the primary self-assembly behavior of free COS-BA was investigated using scanning electron microscopy (SEM) (Fig. 1E), which suggested that COS-BA could form a highly uniform nano-sphere of \sim 168 nm, implying that the chemical modification of COS does not alter the self-assembly ability of BA itself (Supporting Information Fig. S6). It is that property that eventually induces the successful construction of the co-assemblies. Notably, apart from the solid nanostructure confirmed by transmission electron microscopy (TEM), COS-BA/Ce6 NPs showed a distinct shell-structure as free COS-BA NPs, and the average shell thickness was approximately 2.35 nm. The other physicochemical characterization is summarized in Fig. 1F. Besides, COS-BA/Ce6 NPs showed a negative ζ -potential of -5.38 mV and hydrodynamic size of \sim 249 nm, higher than that obtained from SEM (\sim 182 nm). Simultaneously, Ce6 loading and encapsulation efficiencies were 8.1 and 96%, respectively, as determined by high-performance liquid chromatography (HPLC). Also, FT-IR data (Fig. 1G) further confirmed this co-assembly because COS-BA/Ce6 NPs exhibited the characteristic C=N, C–N, and C=CH peaks of Ce6 appearing at 1633, 1078, and 633 cm⁻¹, respectively.

3.2. Co-assembled mechanism and the formation of the shell-structure

Subsequently, to better comprehend the co-assembly mechanism, we first investigated the primary formation process of NPs. We found that the co-assembly of COS-BA with Ce6 may be spontaneous because these two species could also form spherical nanostructure even if without sonication (Supporting Information Fig. S7), which may be due to the negative Gibbs free energy change (ΔG°) in co-assemblies³⁷. This spontaneous assembly also suggested a stronger intermolecular interaction between COS-BA and Ce6. Generally, the intermolecular interactions in supramolecular self (or co-) assemblies are noncovalent π - π stacking, hydrogen bonding, and van der Waals forces^{38,39}. For this analysis, we then investigated the UV absorption of COS-BA/Ce6 NPs (Fig. 1H and F), which suggested a red-shifted Soret (410 nm) and Qy (667 nm) bands compared to free Ce6 (405 and 665 nm, respectively). Meanwhile, the significant red-shifted characteristic absorption of COS-BA can also be found, indicating a possible intermolecular π - π stacking between COS-BA and Ce6⁴⁰. Moreover, after incubating with the surfactant sodium dodecyl sulfate (SDS, 0.2% w/v) (Supporting Information Fig. S8), COS-BA/Ce6 NPs showed a newly blue-shifted Qy band at 641 nm and dramatically recovered fluorescence, demonstrating that the hydrophobic interactions also contributed to the co-assembly²⁸. Since these associative noncovalent interactions, co-assemblies showed remarkable fluorescence quenching (98.2%) in water

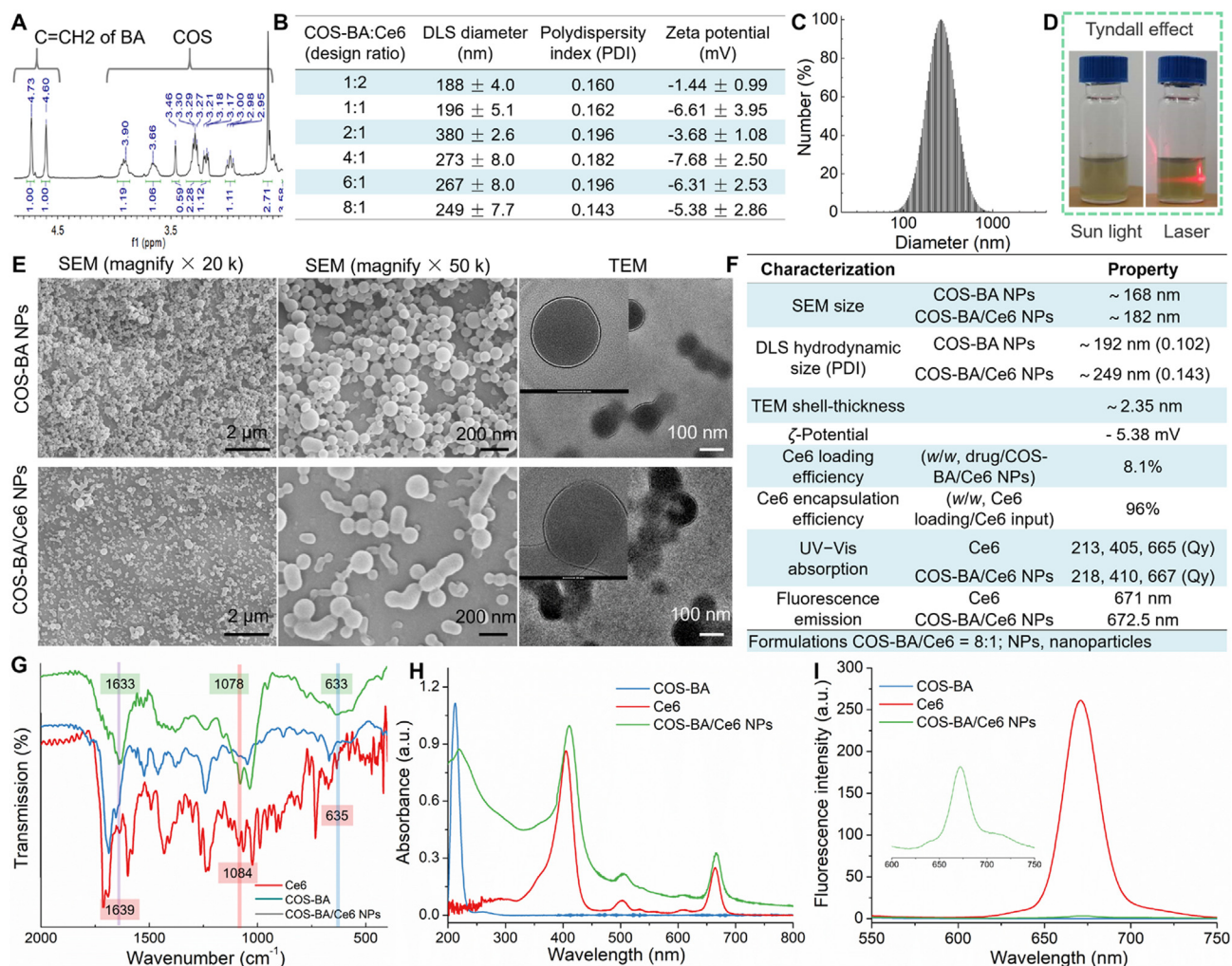


Figure 1 Fabrication and characterization of chitosan oligosaccharides-modified betulinic acid (COS-BA) prodrug-mediated nano-coassemblies COS-BA/Ce6 NPs. (A) The amplified key positions of ^1H NMR of COS-BA. (B) Preparation of co-assembled COS-BA/Ce6 NPs with various COS-BA/Ce6 ratios. (C) Size distribution of COS-BA/Ce6 NPs using COS-BA and Ce6 (molar ratio, 8:1) as building blocks. (D) The water solubility and Tyndall effect of co-assemblies, indicating a colloidal nature. (E) SEM and TEM images of free COS-BA self-assemblies and co-assembled COS-BA/Ce6 NPs. (F) Summary of physicochemical properties of COS-BA/Ce6 NPs. (G) FT-IR spectra, (H) UV-Vis spectra, and (I) fluorescence emission spectra of free Ce6, COS-BA, and co-assembled COS-BA/Ce6 NPs in water.

(Fig. 1I). Collectively, it is reasonable to believe that π - π stacking and hydrophobic interactions may be the main driving forces for the construction of co-assemblies.

Afterward, to further visualize the assembly process more intuitively and reveal the underlying reasons why shell-structured NPs can form, we performed a simplified molecular dynamics (MD) simulation model containing 16 optimized COS-BA molecules and an additional two Ce6 in a water box. Initially, we evaluated the possible interaction/binding of COS-BA self-assemblies within 5 ns of simulation time (Fig. 2A and Supporting Information Fig. S9). We found that, except for numerous of intramolecular hydrogen bonds in the COS fraction, several pairs of intermolecular H-bonds between COS-BA could also be observed (Fig. 2B and Supporting Information Fig. S10), which indicated that hydrogen bonding may be one of the main driving forces for the formation of COS-BA NPs. Particularly and interesting, in COS-BA self-assemblies, all COS-BA molecules form an apparently symmetrical structure (Fig. 2C). This fascinating

phenomenon motivated us to explore the possible relationship between this property and the formation of shell-structured COS-BA NPs. Then, we attempted to expand the units of the box. Surprisingly, the connected boxes consisting of COS-BA molecules were arranged in a regular manner resulting in an “orthogonal” hollow network structures (Supporting Information Fig. S11). More importantly, we randomly calculated the thickness of the shell molecules and found that were consistent with the TEM (~ 2.35 nm) (Fig. 2D). This tendency to form hollow network structures may be responsible for the formation of shell-structured NPs. To test this idea, the MD structure of COS-BA/Ce6 co-assemblies was simulated (Fig. 2E and Supporting Information Fig. S12). Similar to COS-BA self-assemblies, a large number of intramolecular and intermolecular H-bonds also were found in the co-assemblies (Fig. 2F and Supporting Information Fig. S13). Additionally, the possible π - π stacking between C=C of COS-BA and the aromatic ring of Ce6 was observed in the co-assemblies (Fig. 2G), which is consistent with

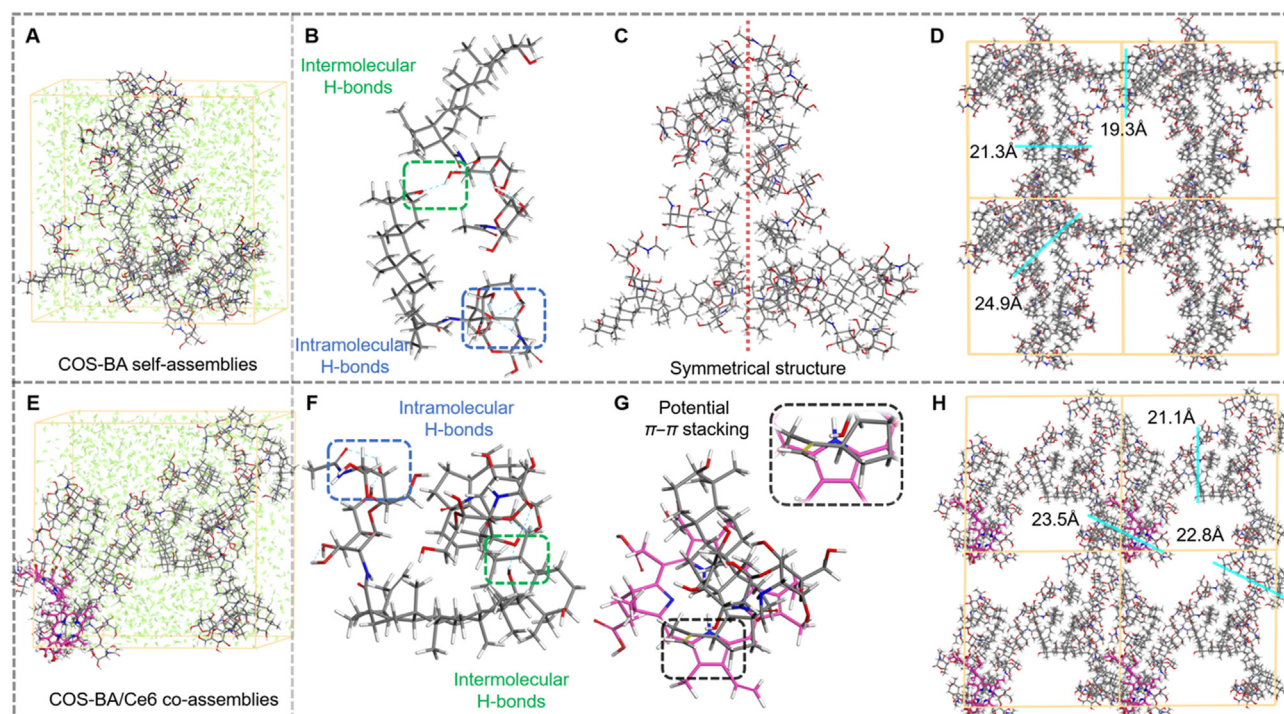


Figure 2 Structures of (A) COS-BA self-assemblies and (E) co-assembled COS-BA/Ce6 NPs after molecular dynamics (MD) simulation for 5 ns with a structural unit molar ratio of 8:1 (COS-BA/Ce6, calculated based on Ce6 loading efficiency). The line model was used for H₂O and the stick models represent COS-BA or Ce6 molecules, where the C atoms of Ce6 are labeled with purple. The hydrogen bond information between COS-BA molecules in (B) its self-assemblies and (F) COS-BA/Ce6 NPs co-assemblies. (C) The apparently symmetrical structure of the COS-BA molecular arrangement after MD simulation. (G) Possible molecular interactions between COS-BA and Ce6 show potential π - π stacking. The indicated thickness of the shell molecules in an “orthogonal” hollow network structure after extending corresponding MD boxes of (D) free COS-BA self-assemblies and (H) COS-BA/Ce6 NPs co-assemblies.

the data from previous UV investigations. After extending the number of boxes, similar hollow network structures can still be found, only with reduced regularity and orthogonality (Supporting Information Fig. S14). This may be the possible reason for the non-uniform morphology of COS-BA/Ce6 NPs compared to COS-BA NPs. Moreover, the molecular shell-layer distance is also close to the shell thickness (~ 2.35 nm) of NPs as seen using the TEM (Fig. 2H). Collectively, we speculated that the formation of shell-structured COS-BA/Ce6 NPs or COS-BA NPs might largely be attributable to this tendency of molecules to assemble into hollow-shell network structures.

3.3. Energy mechanism of enhanced $^1\text{O}_2$ generation

Next, we further examined the generation of singlet oxygen ($^1\text{O}_2$), one of the critical reactive oxygen species (ROS) of PDT performance using DPBF (1,3-diphenylisobenzofuran) as a probe. After sustained irradiation of the mixture solutions of COS-BA/Ce6 NPs with DPBF, the UV absorption of DPBF decreased in intensity, indicating $^1\text{O}_2$ generation (Fig. 3A). After comparison with the methylene blue (MB) reference, the $\Phi(^1\text{O}_2)$ of COS-BA/Ce6 NPs was calculated as 0.26, slightly higher than free Ce6 ($\Phi=0.19$) (Fig. 3B). Generally, the energy absorbed by photosensitizers will undergo three relaxation pathways involving fluorescence, heating effect *via* vibrational relaxation, and ROS generation through an intersystem crossing (ISC)⁴¹. Consistent with the significantly quenched fluorescence emission, COS-BA/

Ce6 NPs also did not promote any heating effect in water (Supporting Information Fig. S15), which implied an enhanced ISC process after co-assembly of Ce6 with COS-BA, thus leading to the improved $^1\text{O}_2$ generation. To further elucidate the molecular mechanism of such an effect, we attempted to optimize and calculate the possible single-molecule model of COS-BA/Ce6 consisting of potential π - π stacking obtained from MD simulation by density functional theory (DFT) (Fig. 3C). Amazingly, COS-BA/Ce6 showed an observable red-shifted UV absorption of 581.24 nm than that of free Ce6 (579.30 nm), indicating the occurrence of π - π stacking (Fig. 3D). Although the energy-minimized geometry of COS-BA/Ce6 showed slight structural differences with inputted MD configuration, the distinctive π -stacking between C=C or C=O bonds of COS-BA with the porphine ring of Ce6 was still observable, further validating that the above π - π stacking is possible. Meanwhile, it has been recently demonstrated that the increased electron-donating efficiency by π - π stacking could facilitate the ISC process⁴², while the ISC rate (K_{ISC}) is proportional to $(1/\Delta E_{\text{ST}})^{2,43}$. That is, the lower energy gap (ΔE_{ST}) of photosensitizer will enhance the ISC process promoting efficient ROS generation. We subsequently calculate the lowest excited singlet state (S_1) and the triplet state (T_1) of Ce6 and COS-BA/Ce6 (Fig. 3E), respectively. The results indicated that COS-BA/Ce6 showed a decreased ΔE_{ST} of 1.1892 eV compared to free Ce6 (1.2001 eV), confirming the enhanced ISC process. The reduction of ΔE_{ST} is helpful for $^1\text{O}_2$ production, which has also been verified in other nano-

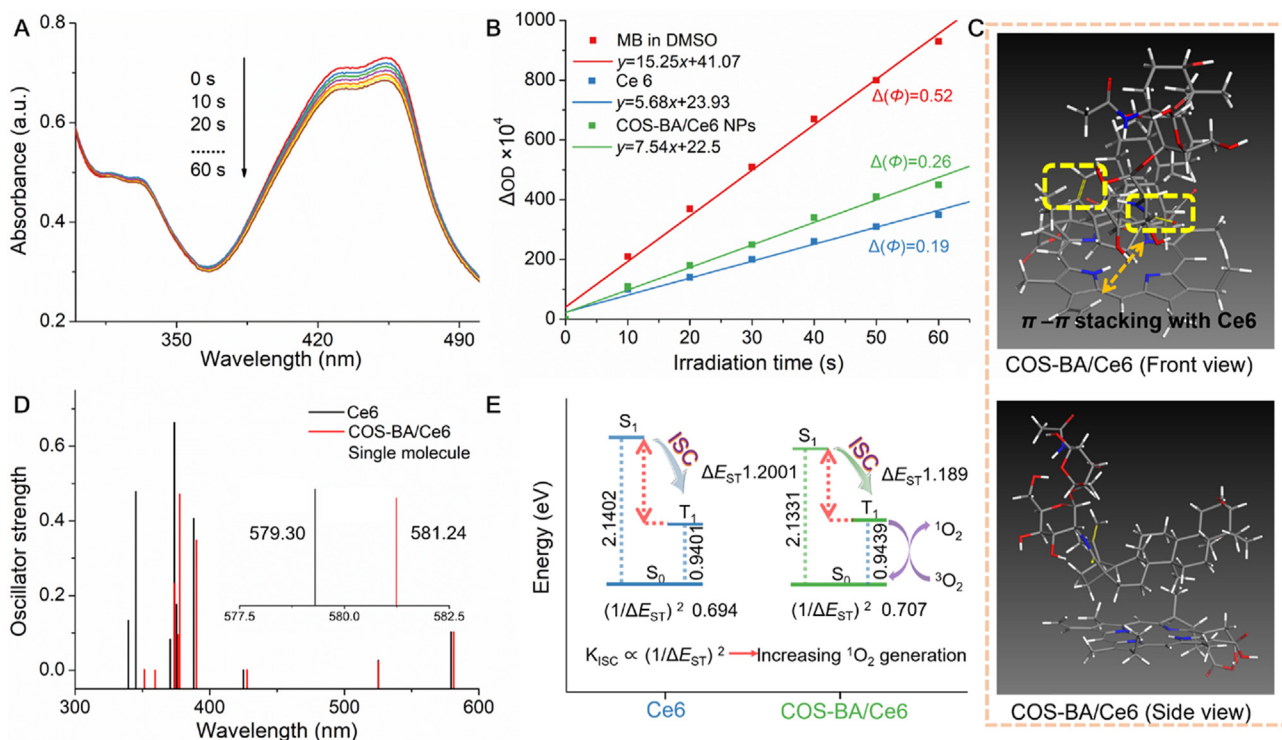


Figure 3 Energy mechanism of improved 1O_2 generation induced by COS-BA/Ce6 NPs. (A) UV–Vis spectra of photodecomposition of 1,3-diphenylisobenzofuran (DPBF) after prolonged irradiation of COS-BA/Ce6 NPs. (B) The first-order plots of DPBF UV absorption changes (ΔOD), the 1O_2 yield was evaluated using methylene blue (MB) ($\Phi = 0.52$) in DMSO as the reference compound. (C) Energy-minimized structures of a possible single-molecule COS-BA/Ce6 model viewed from the side and front, which was obtained according to the initial molecular configuration between Ce6 with COS-BA after MD simulation and following DFT calculations. (D) Predicted UV–Vis absorption spectra transitions (vertical bars) of free Ce6 and an optimized COS-BA/Ce6 model. (E) Calculated energy levels of their lowest excited singlet state (S_1) and lowest triplet state (T_1), respectively, [Gaussian 09/B3LYP/6-31G (d, p)]. Where ΔE_{ST} was calculated as $E_{S_1} - E_{T_1}$.

photosensitizers⁴⁴. Taken together, the π -stacking seems to reduce the ΔE_{ST} of Ce6 after co-assembly with COS-BA, thus leading to improved 1O_2 generation.

3.4. Chemotherapy dormancy characteristics

Afterward, to validate the design concept in the present study that developing amphiphilic COS-BA molecule could effectively increase the therapeutic effect of BA by improving the cell uptake through increasing hydrophilicity, and meanwhile further constructing stimuli-responsive and fully hydrophilic COS-BA/Ce6 NPs facilitated its dormancy in normal tissues and activation in tumor sites. To test this hypothesis, we first investigated the drug release behavior of COS-BA/Ce6 NPs in various buffer solutions (Fig. 4A). The results indicated that COS-BA/Ce6 NPs showed a pH-responsive behavior with a cumulative Ce6 release of 88% at pH 5.6 and 57% at pH 7.4 after 24 h, respectively. This feature likely arose from the destruction of numerous hydrogen bonds that existed in COS-BA/Ce6 NPs after the introduction of acidic H^+ ⁴⁵, thus leading to increased Ce6 release (Fig. 4B). This was further confirmed by the disassembly of COS-BA/Ce6 NPs after incubation in acidic environments directly (Fig. 4C). This pH-responsive feature may be beneficial for an effective antitumor therapy due to the weakly acidic tumor microenvironment³⁴. Meanwhile, COS-BA/Ce6 NPs had better stability because no significant size or PDI changes could be observed after incubation in PBS and 1640-RMPI cell culture medium for 10 days

(Supporting Information Fig. S16), which would be important for their potential use for further biomedical applications.

Subsequently, further investigations were conducted by evaluating the cytotoxicity of free lipophilic BA (contact angle θ : 133.3°) and amphiphilic COS-BA (θ : 52°) (Fig. 4D) by a standard methylthiazoly-diphenylterazolium bromide (MTT) assays. As predicted, either for 4T1 cancer cells or normal LO2 hepatocytes, individual COS has essentially no anticancer activity at relatively low doses. This might be due to the anti-proliferation effects of COS being activated *via* inducing NF- κ B signaling pathway only at high concentrations (approximately at milligram level)³⁰. Whereas, COS-BA performs remarkably enhanced cytotoxicity with extremely low IC_{50} values (6.03 μ g/mL for 4T1 and 9.92 μ g/mL for LO2) compared to those of BA (17.63 μ g/mL for 4T1 and 20.53 μ g/mL for LO2) even at the same mass concentrations (Fig. 4E and J). The elicited results implied that modification of water-soluble COS greatly enhances the cellular uptake efficiency of lipophilic BA, thus leading to the strong anticancer activity of COS-BA. To quantify the uptake efficiency, the accumulation of BA or COS-BA within 4T1 cells was directly determined by HPLC (Supporting Information Fig. S17). The results clearly supported that amphiphilic COS-BA exhibits a significantly higher uptake than free BA (approximately 3.6-fold after 3 h of incubation), demonstrating the enhanced chemotherapeutic activity of COS-BA. The above conclusion was further supported by the significantly improved cytotoxicity of amphiphilic COS-BA against HepG2 and MCF-7 cancer cells (Supporting

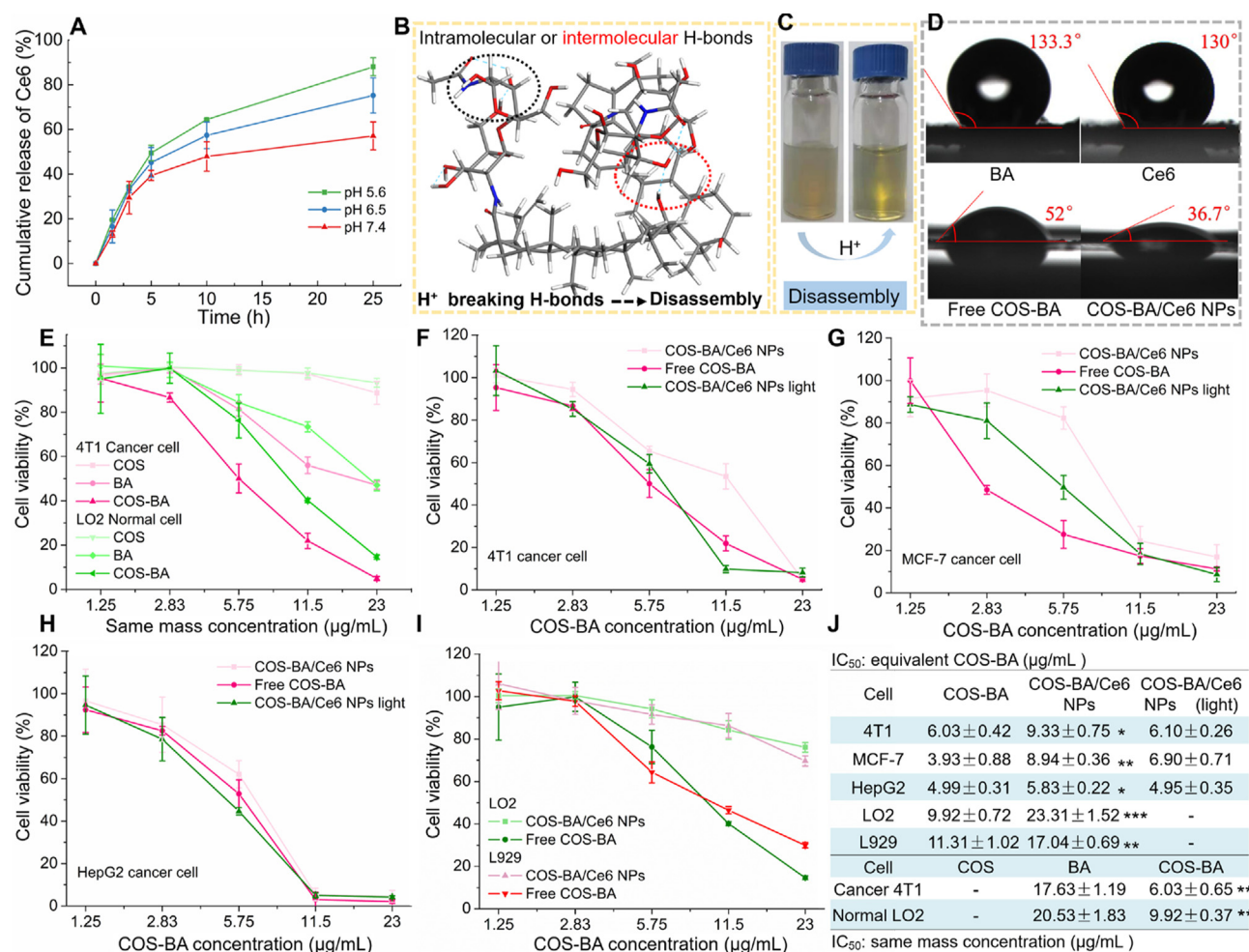


Figure 4 (A) *In vitro* Ce6 release profiles from COS-BA/Ce6 NPs in PBS (pH 7.4, 6.5 or 5.6) containing Tween 80 (0.5%, v/v) at 37 °C. (B) The possible pH-responsive mechanism that H⁺ triggers the disassembly of NPs. (C) The disassembly of COS-BA/Ce6 NPs after direct incubation in approximately pH 4.0 water. (D) The contact angle of free BA, Ce6, COS-BA, and COS-BA/Ce6 NPs, respectively. (E) Cell cytotoxicity of free BA, COS, and amphiphilic COS-BA against representative cancer 4T1 and normal LO2 cells. Cell viability of (F) 4T1, (G) MCF-7, (H) HepG2 cancer cells after being incubated with free COS-BA, COS-BA/Ce6 NPs with/without irradiation at indicated equivalent COS-BA concentration for 24 h. (I) Cell cytotoxicity of free COS-BA, non-irradiated COS-BA/Ce6 NPs against normal LO2 and L929 cells. (J) The IC₅₀ analysis of COS-BA against cancer and normal cells. Data are expressed as means ± SD (*n* = 6). **P* < 0.05, ***P* < 0.01, and ****P* < 0.001 show the significant differences.

Information Fig. S18), which are well consistent with the design concept. After co-assembly with Ce6, we found that COS-BA/Ce6 NPs without irradiation exhibit remarkably inhibited cytotoxicity against 4T1 cancer cells compared to the equivalent COS-BA, especially at 11.5 μg/mL, but the basic PDT activity was not affected (Fig. 4F). To validate this phenomenon more fully, we further investigated the *in vitro* cytotoxicity of COS-BA/Ce6 NPs against other cancer cells including MCF-7 and HepG2. Interesting, amphiphilic COS-BA showed very stronger cytotoxicity against MCF-7 cells (Fig. 4G), but the chemotherapeutic activity decreased significantly after co-assembly with Ce6, *i.e.*, non-irradiated COS-BA/Ce6 NPs. Similar results were also observed in HepG2 cells only with a slight decrease (Fig. 4H). To further support the above conclusions, we also evaluated the chemotherapeutic effects of nano-coassemblies and COS-BA against normal mouse fibroblast L929 cells and human LO2 hepatocytes (Fig. 4I). The results indicated that the assembled COS-BA/Ce6 NPs significantly reduced the original highly toxic amphiphilic drug

COS-BA, showing excellent biocompatibility. By analyzing the cytotoxicity, the IC₅₀ values of the amphiphilic COS-BA were significantly lower than that of the co-assembled COS-BA/Ce6 NPs regardless of cancer or normal cells (Fig. 4J). That is to say, constructing completely hydrophilic and stimuli-responsive nano-coassemblies can effectively suppress the high cytotoxicity of amphiphilic drug COS-BA in advance. Considering the distinctive pH-responsive feature, it seems that COS-BA/Ce6 NPs will be dormant to normal tissues with desired low chemotherapy toxicity, but active to tumor tissues owing to their stimulating release of highly toxic COS-BA in the weakly acidic tumor microenvironment. Taken together, unlike the widely reported nano-functionalization of chemotherapeutic reagents that have enhanced anticancer activity^{22,23}, amphiphilic COS-BA mediated nano-coassemblies not only exhibit a smart “dormancy” characteristic with insidious chemotherapy effects but also retain specialized PDT activity, showing huge potential for smart anti-tumor therapy.

To explore the possible reasons behind this chemotherapy dormancy characteristic, the time-dependent cellular uptake behavior of COS-BA/Ce6 NPs was evaluated successively by incubating with 4T1 cancer cells. The results indicated that, although COS-BA/Ce6 NPs showed remarkable fluorescence quenching, it still showed enhanced phagocytic efficiency compared to free Ce6 owing to the stronger cytoplasmic red fluorescence, as determined by flow cytometry quantitative analysis (Fig. 5A). This improved cellular internalization of NPs may be ascribed to endocytosis²¹. Taken together, we speculated that, although highly water-soluble co-assemblies COS-BA/Ce6 NPs (contact angle θ : 36.7°) exhibited improved cellular endocytosis than lipophilic Ce6 (θ : 132.6°, close to BA), yet the reduced phagocytosis efficiency of NPs might appear compared to amphiphilic COS-BA molecule, thus appearing suppressed the chemotherapeutic cytotoxicity of COS-BA/Ce6 NPs. That is to say, the cell uptake efficiency from high to low as such sequence: amphiphilic COS-BA, hydrophilic COS-BA/Ce6 NPs, lipophilic BA or Ce6. More importantly, the inadequate disassembly of cellular NPs may be another important reason for the weakened chemotherapeutic effect, all of which may be related to the smart chemotherapy dormancy of COS-BA/Ce6 NPs. Besides, because that the disassembly of NPs was specifically conducted in the acidic environment of tumor cells, to demonstrate the pH-responsive feature, we further attempted to compare the uptake effects of COS-BA/Ce6 NPs in normal LO2 cells (Fig. 5B). However, COS-BA/Ce6 NPs did not exhibit significantly inhibited Ce6 red fluorescence in LO2 cells. In contrast, the uptake behavior by LO2 was similar to that of 4T1 cancer cells, suggesting that COS-BA/Ce6 NPs can also disassemble even in normal cells, which may result from the weakly acidic pH intracellular compartments (endosomes/lysosomes) existing inside both cancer and normal cells⁴⁶. Since the cellular uptake of NPs depends on the process of endocytosis, the direct drug incubation might not highlight the pH-responsiveness of COS-BA/Ce6 NPs at the cellular level. Nevertheless, the tumor microenvironment (TME) is highly acidic compared to normal tissues⁴⁷. Regardless of cancer intracellular or TME, COS-BA/Ce6 NPs can be pH-responsive and disassembled to trigger the release of highly toxic COS-BA. Whereas, in normal tissues, COS-BA/Ce6 NPs could only be disassembled after entering normal cellular environment, reducing the probability of COS-BA release. Therefore, we infer the chemotherapy dormancy characteristic of COS-BA/Ce6 NPs to the tumor microenvironment is valid and reliable, and the design idea in the present study is feasible.

3.5. *In vitro* chemotherapy/PDT anticancer efficacy of COS-BA/Ce6 NPs

Additionally, prior to detailed *in vitro* chemotherapy/PDT anticancer efficacy of COS-BA/Ce6 NPs and to further uncover the endocytosis mechanism, we study the four main endocytosis pathways by adding corresponding endocytic inhibitors including chlorpromazine (clathrin-mediated), chloroquine phosphate (lysosome acidification inhibitor), nystatin (caveolae-mediated), and a macropinocytosis inhibitor EIPA (ethylisopropyl amiloride) (Fig. 5C and D). We observe that the introduction of nystatin and chlorpromazine could more efficiently inhibit phagocytic efficiency than EIPA and chloroquine phosphate, showing significantly decreased cellular fluorescence compared with normal 37 °C. These results indicated that COS-BA/Ce6 NPs were

internalized by multiple mechanisms, mainly through the clathrin and caveolae-mediated endocytosis pathways.

Since the increased ¹O₂ generation *via* intermolecular interactions, COS-BA/Ce6 NPs exhibits significantly enhanced intercellular ROS yield than that of Ce6 as indicated by the stronger green fluorescence of DCFH probe (Fig. 5E), implying the higher photodynamic efficiency. MTT assays demonstrate that COS-BA/Ce6 NPs under irradiation perform a remarkably enhanced inhibition effect on 4T1 cells than that of equivalent Ce6, while with relatively moderate cytotoxicity without irradiation (Fig. 5F). Significantly, the IC₅₀ of Ce6 (0.53 μg/mL) in COS-BA/Ce6 NPs was much lower than free Ce6 (1.39 μg/mL) (Fig. 5G), suggesting remarkably improved PDT efficacy, which was further perfectly demonstrated by the cytotoxicity of COS-BA/Ce6 NPs against human MCF-7 and HepG2 cancer cells (Supporting Information Fig. S19). Likewise, by comparison with free Ce6, the relative lower IC₂₅, IC₅₀, and IC₇₅ values were also observed in co-assemblies (Fig. 5G). Meanwhile, compared with Ce6 PDT alone and single chemotherapy of NPs in the dark, COS-BA/Ce6 NPs under irradiation achieved more effective combined chemotherapy/PDT against the above three cancer cells, showing a synergism (combination index: CI < 1) (Fig. 5I). Besides, the live/dead cell fluorescence dual staining using calcein-acetoxymethyl ester (calcein-AM) and propidium iodide (PI) further confirmed that COS-BA/Ce6 NPs could efficiently induce cell apoptosis and necrosis, as the treated cells were almost stained with red PI fluorescence signal when cultured for an additional 10 h after irradiation (Fig. 5H). Meanwhile, non-irradiated COS-BA/Ce6 NPs (higher dose Ce6: 3.2 μg/mL) also had certain chemotherapeutic activity as seen by the AM and PI signals simultaneously. This remarkably improved PDT activity of COS-BA/Ce6 NPs was further validated by the AM/PI staining after treatment for an additional 20 h (Supporting Information Fig. S20). Moreover, when adding sodium azide (SA) and D-mannitol (DM), a separately special quencher of ¹O₂ and ·OH⁴⁸, to the COS-BA/Ce6 NPs-PDT-treated 4T1 cells, the obviously increased cell viability implied that Type I (·OH) and Type II (¹O₂) photoreactions occurred simultaneously in COS-BA/Ce6 NPs-mediated PDT process (Fig. 5J). Furthermore, COS-BA/Ce6 NPs particularly possess better blood compatibility as indicated by the negligible red blood cells hemolysis (Fig. 5K), suggesting the potential for biomedical applications *via* intravenous administration.

3.6. *In vivo* biodistribution of COS-BA/Ce6 NPs

Subsequently, prior to *in vivo* distribution investigation, we next assessed the pharmacokinetics of COS-BA/Ce6 NPs by monitoring the Ce6 concentration in the blood after injection intravenously with equivalent Ce6 or COS-BA/Ce6 NPs. The Ce6 concentration–time profiles in the blood (Fig. 6A) and the comparative pharmacokinetic parameters (Supporting Information Table S1) clearly support that COS-BA/Ce6 NPs have a prolonged circulation in the bloodstream, which may allow for greater accumulation at tumor sites. In particular, COS-BA/Ce6 NPs showed quick blood elimination within 2 h, implying favorable biodegradability. Accordingly, we then investigated the *in vivo* biodistribution and tumor accumulation ability of COS-BA/Ce6 NPs (Fig. 6B and C). Similar to universally reported Ce6 nanocomposites³³, COS-BA/Ce6 NPs can be distributed rapidly throughout the whole body. Especially during the first 4 h, co-assemblies exhibited obvious stronger fluorescence emission at

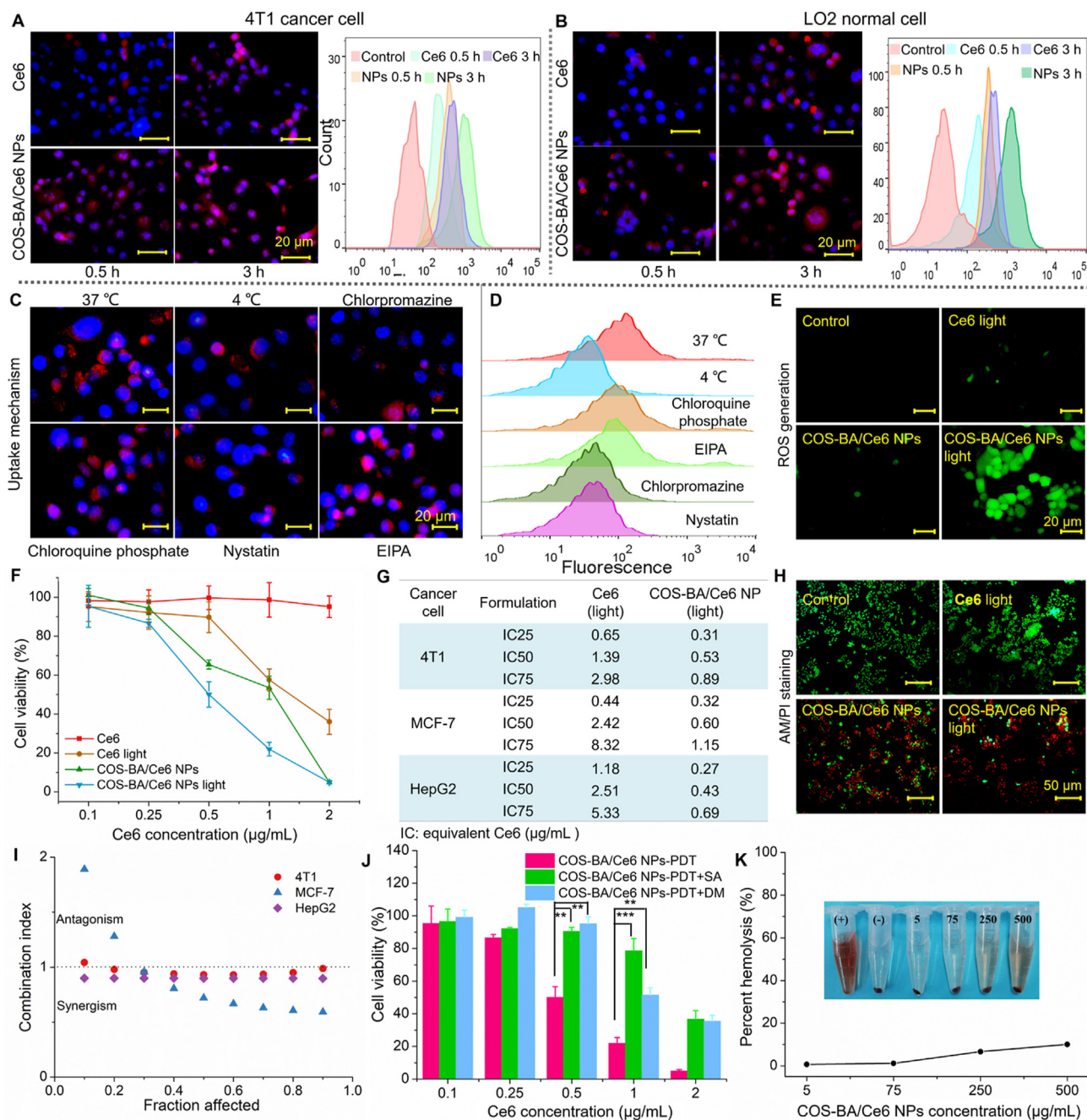


Figure 5 *In vitro* anticancer efficacy of COS-BA/Ce6 NPs. Cellular internalization of (A) 4T1 cancer cells and (B) LO2 normal cells incubated in free Ce6 or COS-BA/Ce6 NPs for 0.5 and 3 h, and corresponding flow cytometric analysis of fluorescence intensity. (C) Uptake inhibition of specific endocytic pathway studies and (D) corresponding fluorescence intensity of cells measured by flow cytometry after incubation with COS-BA/Ce6 NPs with/without endocytic inhibitors including chlorpromazine, chloroquine, nystatin, and ethylisopropyl amiloride (EIPA). Scale bars = 20 µm. (E) Cellular ROS generation induced by free Ce6 or COS-BA/Ce6 NPs (equivalent Ce6: 1.6 µg/mL). Scale bars = 20 µm. (F) Cell viability of 4T1 cells after various treatments for 24 h. (G) The IC₂₅, IC₅₀, IC₇₅ analysis of free Ce6 and COS-BA/Ce6 NPs against 4T1, MCF-7, and HepG2 cells, respectively. (H) Calcein-AM/propidium iodide (PI) live/dead staining of COS-BA/Ce6 NPs (Ce6: 1.6 µg/mL)-treated 4T1 cells after incubation for additional 10 h, as well as non-irradiated COS-BA/Ce6 NPs (Ce6: 3.2 µg/mL). Scale bars = 50 µm. (I) Combination index (CI) of COS-BA/Ce6 NPs on 4T1, MCF-7, and HepG2 cells, as determined by Chou–Talalay theorem calculation. (J) PDT mechanisms (Type I and Type II) induced by irradiation of COS-BA/Ce6 NPs and evaluated by specific ¹O₂ and ·OH quencher sodium azide (SA) and D-mannitol (DM), respectively. (K) Percent hemolysis of red blood cells after incubation with COS-BA/Ce6 NPs for 4 h. Data are expressed as means ± SD (n = 3). *P < 0.05, **P < 0.01, and ***P < 0.001 show the significant differences.

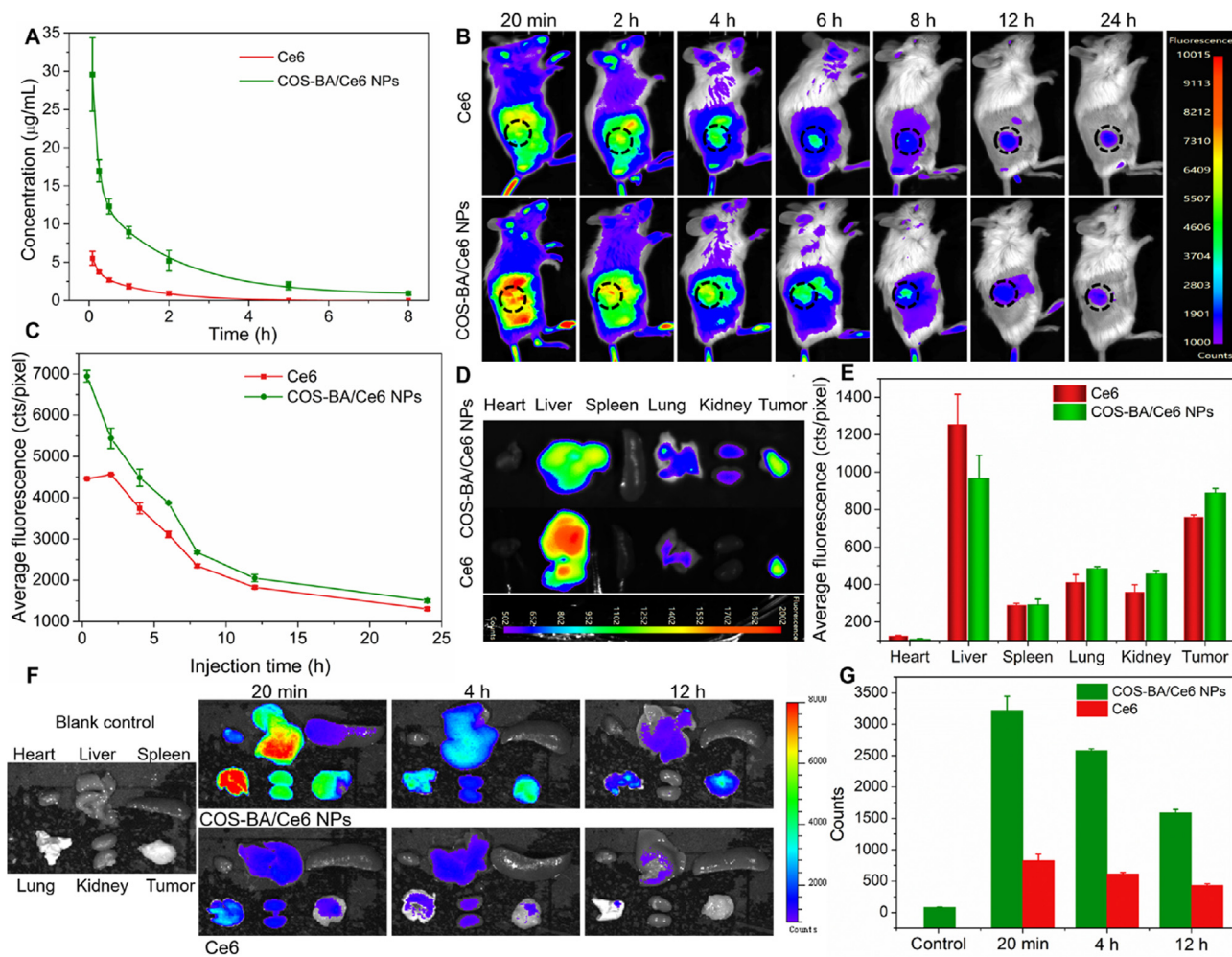


Figure 6 *In vivo* blood circulation and biodistribution of COS-BA/Ce6 NPs. (A) Ce6 concentration–time profiles in the blood after i.v. injections of equivalent Ce6 or co-assembled COS-BA/Ce6 NPs ($n = 3$). (B) Whole-body fluorescence images of 4T1 tumor-bearing mice after i.v. injections of indicated drugs at various time points. (C) Average fluorescence intensity obtained from the tumor sites in (B). (D) *Ex vivo* fluorescence images of tumors and major organs excised from the above mice at 24 h, and corresponding (E) fluorescence intensity quantitative result ($n = 3$). (F) *Ex vivo* fluorescence images of tumors and major organs at different times after i.v. injections of Ce6 or COS-BA/Ce6 NPs, and (G) corresponding fluorescence intensity analysis of tumors. Data are expressed as means \pm SD ($n = 3$).

tumor sites than free Ce6, suggesting the improved retention and tumor-targeted accumulation ability of COS-BA/Ce6 NPs, probably attributed to the passive enhanced permeability retention (EPR) effect afforded by the nanoparticles¹⁴. After 6 h post-injection, the fluorescence intensity at tumor sites gradually decreased rapidly. Notably, unlike the commonly reported nanocomposites with significantly enhanced tumor accumulation compared to free positive drug²⁹, COS-BA/Ce6 NPs did not show very prominent accumulation at tumor sites at 24 h post-injection than free Ce6 (Fig. 6C), which was further supported by the imaging of the excised tumor (Fig. 6D and E). The excellent biodegradability of NPs may be responsible for the introduction of natural small organic molecules. This was also observed with other terpenoids small molecule-mediated nano-assemblies⁴⁹. Besides, COS-BA/Ce6 NPs also showed a similar tissue distribution as free Ce6 (Fig. 6E), and the *ex vivo* average fluorescence intensity was generally lower than that presented *in vivo*, further implying the good biodegradability. Additionally, considering the close fluorescence level difference between 2 and 4 h after

injection of NPs and Ce6, as well as experimental operability allowing sufficient intervals for irradiation, 4 h after administration was chosen as the light time point for subsequent PDT therapy.

Considering the not very prominent tumor accumulation at 24 h than free Ce6, to further validate the increased EPR effect that COS-BA/Ce6 NPs do have, we immediately monitored the *ex vivo* fluorescence images of tumors at different times after injection intravenously with nanodrugs (Fig. 6F and G). Remarkably, either at 20 min or at 12 h post-injection, COS-BA/Ce6 NPs indeed showed strong fluorescence emission at tumor sites than free Ce6, demonstrating the excellent and enhanced tumor accumulation ability. Meanwhile, as time passed, the fluorescence intensities retained in tumor tissue gradually weakened (Fig. 6G), which is entirely consistent with the results of *in vivo* animal fluorescence imaging. Clearly, this rapid biological metabolism and enhanced tumor accumulation avoided potential long-term accumulation toxicity, guaranteeing highly efficient antitumor therapy with better biosafety.

3.7. *In vivo* chemotherapy/PDT combinatorial anti-tumor treatment

Motivated by the unique dormancy characteristic, good biodegradability, and PDT activity, the *in vivo* chemotherapy/PDT combination antitumor therapy was investigated. 4T1 tumor-bearing mice were randomly divided into 6 groups and injected intravenously with equivalent Ce6 (3.5 mg/kg of body) every 2 days for a total of three doses. 4 h post-injection, the tumor sites of mice in the light groups were irradiated for 15 min (Fig. 7A). Meanwhile, corresponding tumor volumes or body weights were recorded every other day. After 14 days of treatment (Fig. 7B), free Ce6 with irradiation and free COS-BA were ineffective in tumor suppression, likely due to the limited drug accumulation in tumor tissue. In contrast, after irradiation of COS-BA/Ce6 NPs, the most significant tumor inhibition was observed, validating the excellent chemotherapy/PDT combination efficiency. The average tumor weights (Fig. 7D) and corresponding photographs of dissected tumors (Fig. 7E) both demonstrated the best antitumor

efficacy of COS-BA/Ce6 NPs under irradiation, as treated mice showed the smallest tumor sizes than those of other groups. The mean tumor inhibition ratio of PDT-treated COS-BA/Ce6 NPs reached 80.3%, higher than those of free Ce6 PDT (42.4%), and free COS-BA (38.5%). Notably, although previous *in vitro* studies have shown that COS-BA/Ce6 NPs without light showed a dormant function of chemotherapeutic activity, it still performs an enhanced antitumor efficiency (49.5%) compared to free COS-BA (Fig. 7D). We speculated that two possible reasons contribute to this result, one is the higher tumor accumulation of COS-BA/Ce6 NPs due to the widely reported EPR effect. Another factor is the weakly acidic tumor microenvironment that stimulated the release of highly toxic COS-BA. Because of the higher critical micelle concentration (CMC, 187 $\mu\text{g}/\text{mL}$) of COS-BA (Supporting Information Fig. S21), it could exist in the monomer state in the tumor environment, thus favoring the improved chemotherapy of non-irradiated COS-BA/Ce6 NPs. Besides, to further verify the superior anticancer efficacy of COS-BA/Ce6 NPs, hematoxylin and eosin (H&E) staining of tumors were performed (Fig. 7G).

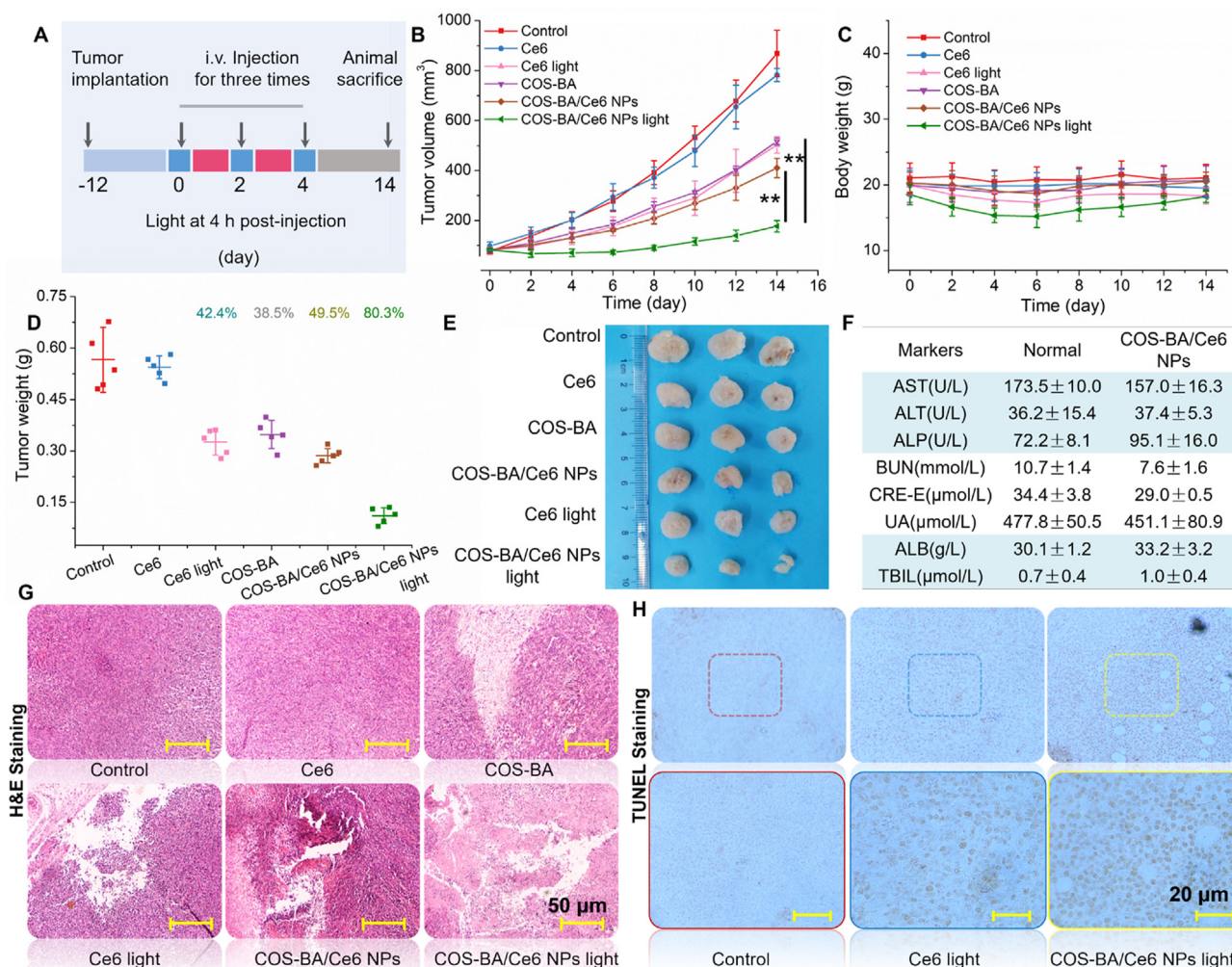


Figure 7 Efficacy study with a subcutaneous 4T1 xenograft model. (A) Schematic illustration of *in vivo* PDT treatment. (B) Tumor growth profiles, (C) body weight changes, and (D) excised tumor weights containing tumor inhibition ratios of 4T1-bearing mice after various treatments in the indicated groups ($n = 5$ for each group). (E) Images of excised tumors from representative mice after treatment. (F) Serum biochemistry analysis after treatment with COS-BA/Ce6 NPs for 14 days. (G) Representative H&E staining of excised tumor sections after different treatments. Scale bars = 50 μm . (H) TUNEL staining of free Ce6 and COS-BA/Ce6 NPs PDT-treated tumor sections. Scale bars = 20 μm ** $P < 0.01$ indicates the significant differences.

The results indicated that COS-BA/Ce6 NPs-PDT-treated tumor sections showed serious tissue deterioration and nuclei deficiency, while moderate tissue necrosis was observed in the other groups. Simultaneously, compared with free Ce6 light, COS-BA/Ce6 NPs under irradiation remarkably increased the number of TUNEL-positive cells showing a stronger brown nuclear staining (Fig. 7H), further confirming the excellent chemotherapy/PDT combination therapy. Moreover, no obvious variations of body weights were observed in all groups (Fig. 7C). Even if the COS-BA/Ce6 NPs or Ce6 light groups had a modest loss in body weight during administration, the body weights returned to normal after a few days. No evident damage or inflammatory lesion could be found in the major organs harvested at the end of treatments (Supporting Information Fig. S22), both indicating the low/no systemic toxicity and good biosafety of COS-BA/Ce6 NPs. Furthermore, although COS-BA/Ce6 NPs are mainly accumulated in liver tissue, the corresponding liver function markers (ALT, AST, and ALP) did not show significant changes compared to normal healthy mice (Fig. 7F), suggesting better biocompatibility. In addition, the renal function markers (BUN, CRE, and UA) and biochemical parameters (ALB, and TBIL) also appeared to be similar to normal mice, further implying better biosafety. Clearly, this prodrug organic small molecule COS-BA-mediated co-assemblies COS-BA/Ce6 NPs possess multiple favorable therapeutic features that open up attractive possibilities for applications in clinical medicine.

3.8. Antitumor immunity of combined chemotherapy/PDT and anti-PD-L1 blockade

Recently, numerous innovative studies have shown that the combination of cancer immunotherapy with other treatment modalities could effectively rouse tumor-specific immune responses to the elimination of primary or distant tumors¹. Encouraged by the unique chemotherapy dormancy function and excellent chemotherapy/PDT antitumor efficacy of COS-BA/Ce6 NPs, we thus wonder whether it could also trigger immunological responses with the assistance of an immune adjuvant anti-PD-L1 to cause highly efficient antitumor therapy. Could it treat distant tumors that cannot be treated directly using PDT treatment, thereby providing an alternative strategy for clinical anticancer applications?

To test this hypothesis, in this study, a “two tumors” model was established and detailed experiment procedures were shown in Fig. 8A. Typically, two 4T1 tumors were inoculated in both the left and right flanks of each mouse. Considering that anti-PD-L1 alone does not have a conspicuous immunotherapeutic effect⁵⁰, the experiments were divided into 5 groups including an untreated group, COS-BA/Ce6 NPs, COS-BA/Ce6 NPs with anti-PD-L1, COS-BA/Ce6 NPs with light, COS-BA/Ce6 NPs with light and anti-PD-L1. After a single i.v. injection of NPs (Ce6: 3.5 mg/kg), the right tumors (primary tumor) in the light groups were irradiated for 15 min to evaluate the immunological effects of PDT/chemotherapy, while the left tumors (distant tumors) in all groups without any treatment were selected for individual chemotherapy. Subsequently, on Days 2, 4, and 6, mice in the immune groups were i.v. injected with anti-PD-L1 antibody (15 µg per mouse per injection) for a total of three doses. Significantly, regardless of PDT treatment or not, COS-BA/Ce6 NPs plus anti-PD-L1 could efficiently inhibit the primary tumor progression (Fig. 8B). And corresponding average tumor inhibition ratios separately reached 86.7% (irradiation) and 76.5% (no irradiation), far higher than

individual chemotherapy (5.7%) or chemotherapy/PDT (27.4%) treatment (Fig. 8C). The photographs of dissected tumors (Fig. 8D) and 4T1-bearing mice (Supporting Information Fig. S23) after 14 days of treatment also visually supported the above conclusion. These results suggested that both NPs-based chemotherapy and chemotherapy/PDT could effectively activate antitumor immunity. Meanwhile, most strikingly, anti-PD-L1 blockade plus NPs also offered a remarkable tumor inhibition effect to non-irradiated distant (left) tumors (Fig. 8E and F), generally stronger than COS-BA/Ce6 NPs alone, which was also confirmed by the corresponding dissected tumors and mice images after treatment (Fig. 8D and Fig. S23), further demonstrating the efficient antitumor immune response induced by COS-BA/Ce6 NPs.

To fully explore this efficient antitumor immune response, CD8⁺ cytotoxic T lymphocytes (CTLs), a critical immunocyte for cancer immunotherapy⁴, were further evaluated by analyzing the immune cells in the right or left tumors after 14 days of treatment. It was found that COS-BA/Ce6 NPs plus anti-PD-L1 with or without PDT treatment induced robust CD8⁺ CTLs infiltration in the primary tumors (Fig. 8H and J). The CD8⁺ CTL infiltration was up to 11.3% after COS-BA/Ce6 NPs-based chemotherapy/PDT plus anti-PD-L1 treatment, slightly higher than COS-BA/Ce6 NPs plus anti-PD-L1 (9.63%), and much higher than that in other groups without anti-PD-L1, including treatment with COS-BA/Ce6 NPs-based chemotherapy (5.12%) or chemotherapy/PDT alone (4.07%). Similarly, compared to non-immune groups, significantly increased CTLs infiltration was also observed in the left (distant) tumors for mice after COS-BA/Ce6 NPs plus anti-PD-L1 with or without PDT treatment (Fig. 8I and K), further implying highly effective immune responses induced by chemotherapy or chemotherapy/PDT combination therapy. Meanwhile, after the introduction of anti-PD-L1, both COS-BA/Ce6 NPs-based chemotherapy and chemotherapy/PDT lead to robust production of multiple cytokines that play pivotal roles in regulating the cytotoxic functions of CTLs⁸, including tumor necrosis factor- α (TNF- α) (Fig. 8L) and interferon- γ (IFN- γ) (Fig. 8M) in the serum samples of mice after 14 days of treatment, further supporting that there were efficient antitumor immune responses. Besides, no apparent changes in body weights were observed in different treatment groups (Fig. 8N), indicating the favorable biosafety of this combined chemotherapy/PDT/immunotherapy.

Taken together, we found that although anti-PD-L1 plus COS-BA/Ce6 NPs with light showed a slightly higher tumor inhibition ratio (86.7%) than the non-irradiated group (76.5%) against the right tumors owing to the influence of PDT (Fig. 8B–D), no significant differences in therapeutic effects on the left tumors was observed in the presence (77.8%) or absence (78.4%) of PDT (Fig. 8E–G). We speculate the following possible reasons lead to this phenomenon. Firstly, for the mechanism of chemotherapy or PDT enhancing the immunological effects of anti-PD-L1 checkpoint blockade, accumulating studies have demonstrated that these treatment modalities could trigger acute inflammation in the tumor area, thereby increasing the presentation of tumor-associated antigens to T cells, thus inducing cancer cells to undergo ICD^{8,9}. Tumor cells undergoing ICD would up-regulate “eat me” signals by exposing the calreticulin (CRT) on the surfaces of immunogenically dying tumor cells and “danger” signals by releasing high-mobility group box 1 (HMGB1), promoting activation of dendritic cells to activate CTLs, whose activity could be enhanced by anti-PD-L1, thus resulting in significantly improved anticancer immunotherapy⁵¹.

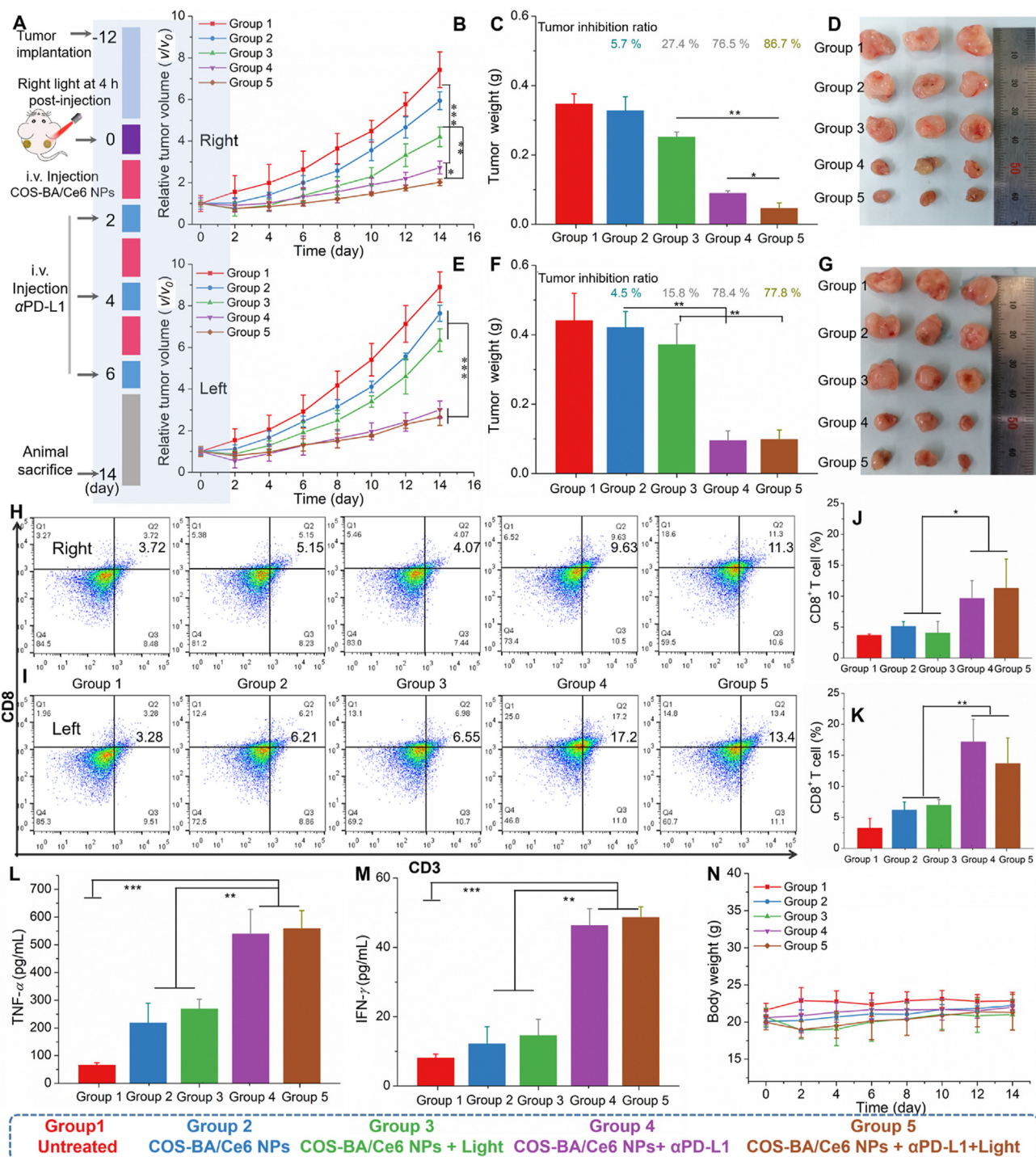


Figure 8 Anti-tumor effect of COS-BA/Ce6 NPs-based chemotherapy/PDT plus checkpoint blockade anti-PD-L1 immunotherapy. (A) Schematic illustration of CNPs-based chemotherapy/PDT with anti-PD-L1 therapy. (B–D) (B) The tumor growth profiles, (C) average tumor weights, and (D) images of excised tumors from representative mice for primary (right) tumors after various treatments for 14 days as indicated. (E–G) (E) The tumor growth curves, (F) average tumor weights, and (G) images of excised tumors for non-irradiated distant (left) tumors after different treatments as indicated. (H) Populations of CD8⁺ T cells in right tumors and (J) percentages of CTL infiltration were quantitatively detected by flow cytometry after 14 days of treatment. (I,K) Populations of CD8⁺ T cells in left tumors on Day 14 were quantitatively detected by flow cytometry ($n = 3$). Secretion of cytokines in sera after 14 days of treatment including (L) IFN- γ and (M) TNF- α measured by ELISA assay ($n = 3$). (N) Changes in mice body weight during various treatments. * $P < 0.05$, ** $P < 0.01$, and *** $P < 0.001$ show the significant differences.

Secondly, in this work, COS-BA/Ce6 NPs could be distributed on the left and right tumors simultaneously, both the left chemotherapy and the right chemotherapy/PDT have huge potential to induce tumor cells undergoing ICD. Meanwhile, COS-BA/Ce6 NPs are administered in only one dose, the immunotherapy mainly depends on three doses of anti-PD-L1, whether chemotherapy or chemotherapy/PDT, they are only primers. The therapeutic differences in inducing tumor cells ICD between individual chemotherapy and combined chemotherapy/PDT treatments might not be very prominent. The percentage of CD8⁺ CTLs on the left (Fig. 8I and K) and right tumors (Fig. 8H and J) also supported the above speculation, no significant difference of CD8⁺ CTLs was observed in the presence or absence of PDT. Therefore, COS-BA/Ce6 NPs plus anti-PD-L1 with or without irradiation achieved similar anticancer efficiency against the left tumors. Furthermore, because 4T1 cells express low levels of PD-L1⁵², anti-PD-L1 alone has been widely proved to have any conspicuous immunotherapeutic effect on 4T1 breast cancers^{53,54}. Despite the ICD effects mediated by COS-BA/Ce6 NPs warrant further investigation, the presented results have shown that COS-BA/Ce6 NPs achieve remarkably enhanced immune responses with the assistance of anti-PD-L1. Collectively, it seems that COS-BA/Ce6 NPs indeed potentiated the cancer immunotherapy of anti-PD-L1, not just a combination therapy.

Although anti-PD-L1 plus COS-BA/Ce6 NPs with or without PDT treatment did not show significant differences in therapeutic effects, both of them showed obviously enhanced antitumor efficacy compared to one dose of COS-BA/Ce6 NPs. That is to say, even if without light treatment, once the immune adjuvant anti-PD-L1 was introduced, the immunogenicity of tumor residues after COS-BA/Ce6 NPs chemotherapy can be boosted resulting in remarkable systemic antitumor immune responses, thus leading to effective suppression of primary or distant tumors. Thus, it should be possible to eliminate primary and metastatic tumors during clinical anticancer immunotherapy with repeated treatments with NPs. Clearly, these results collectively provide evidence of highly effective and synergistic antitumor immune responses induced by COS-BA/Ce6 NPs in combination with an anti-PD-L1 blockade, with either chemotherapy alone or in the combination of chemotherapy/PDT.

4. Conclusions

In summary, we purposefully designed, synthesized, and developed a biocompatible, biodegradable, low toxic but highly efficient and clinically available transformed photo-chemotherapeutic nano-prodrug COS-BA/Ce6 NPs by combining three multifunctional components—a self-assembled natural small molecule betulinic acid (BA), a water-soluble COS, and a low toxic photosensitizer Ce6 for combined chemotherapy/PDT. It subsequently triggers highly effective and synergistic antitumor immune responses in combination with an anti-PD-L1 blockade, with either chemotherapy alone or in the combination of chemotherapy/PDT. Specially, we show that hollow network molecular arrangement might facilitate the formation of shell-structured nanoparticles. Modifications of water-soluble COS could greatly enhance the anticancer activity of lipophilic natural small molecules through constructing an amphiphilic prodrug. We also show that the resulting nanodrugs showed multiple favorable therapeutic features, especially a smart “dormancy” function with insidious chemotherapy effects. Combined with the distinctive pH

responsiveness, these co-assemblies perform low toxicity and biosafety with normal tissue, but are highly toxic to tumor tissues. Together with the improved ¹O₂ generation, good biodegradability, and biocompatibility, all of which contributed to the highly efficient, synergistic, and secure anticancer chemotherapy/PDT/immunotherapy. In particular, the individual chemotherapy without PDT treatment can activate systemic antitumor immune responses, opening up attractive possibilities for clinically synergistic anticancer chemotherapy-immunotherapy. Overall, this work provides a promising insight for developing natural multifunctional highly bioactive and low toxic nano-immunostimulants for clinical immunotherapy.

Acknowledgments

We greatly acknowledge the financial support from the National Natural Science Foundation of China (No. 31972040, 81760708). Jiangxi Provincial Natural Science Foundation Key Project (No.20192ACBL20028, China).

Author contributions

Xin Yang and Jianjun Cheng conceived and designed the project. Jianjun Cheng, Haitian Zhao and Bin Li contributed equally to this work. Jianjun Cheng carried out the experiments and performed data analysis. Haitian Zhao, Hua Zhang, Qianyu Zhao, Shiyao Fu and Ying Han participated part of the experiments. Bin Li, Weihong Lu and Xin Yang provided experimental drugs and quality control. Jiahua Shi provided the experiment support during revision. All of the authors have read and approved the final manuscript.

Conflicts of interest

The authors have no conflicts of interest to declare.

Appendix A. Supporting information

Supporting data to this article can be found online at <https://doi.org/10.1016/j.apsb.2022.06.008>.

References

1. Sang W, Zhang Z, Dai YL, Chen XY. Recent advances in nanomaterial-based synergistic combination cancer immunotherapy. *Chem Soc Rev* 2019;**48**:3771–810.
2. Li XY, Guo XM, Ling JB, Tang Z, Huang GN, He LZ, et al. Nanomedicine-based cancer immunotherapies developed by reprogramming tumor-associated macrophages. *Nanoscale* 2021;**13**:4705–27.
3. Chao Y, Xu LG, Liang C, Feng LZ, Xu J, Dong ZL, et al. Combined local immunostimulatory radioisotope therapy and systemic immune checkpoint blockade imparts potent antitumour responses. *Nat Biomed Eng* 2018;**2**:611–21.
4. Wen YY, Chen X, Zhu XF, Gong YC, Yuan GL, Qin XY, et al. Photothermal-chemotherapy integrated nanoparticles with tumor microenvironment response enhanced the induction of immunogenic cell death for colorectal cancer efficient treatment. *ACS Appl Mater Interfaces* 2019;**11**:43393–408.
5. Peng JR, Xiao Y, Yang Q, Liu QY, Chen Y, Shi K, et al. Intracellular aggregation of peptide-reprogrammed small molecule nanoassemblies enhances cancer chemotherapy and combinatorial immunotherapy. *Acta Pharm Sin B* 2021;**11**:1069–82.

- Song W, Kuang J, Li CX, Zhang MK, Zheng DW, Zeng X, et al. Enhanced immunotherapy based on photodynamic therapy for both primary and lung metastasis tumor eradication. *ACS Nano* 2018;**12**: 1978–89.
- Wang C, Xu LG, Liang C, Xiang J, Peng R, Liu Z. Immunological responses triggered by photothermal therapy with carbon nanotubes in combination with anti-CTLA-4 therapy to inhibit cancer metastasis. *Adv Mater* 2014;**26**:8154–62.
- He CB, Duan XP, Guo NN, Chan C, Weichselbaum RR, et al. Core-shell nanoscale coordination polymers combine chemotherapy and photodynamic therapy to potentiate checkpoint blockade cancer immunotherapy. *Nat Commun* 2016;**7**:12499.
- Galluzzi L, Buque A, Kepp O, Zitvogel L, Kroemer G. Immunogenic cell death in cancer and infectious disease. *Nat Rev Immunol* 2017;**17**: 97–111.
- Chiang CS, Lin YJ, Lee R, Lai YH, Cheng HW, Hsieh CH, et al. Combination of fucoidan-based magnetic nanoparticles and immunomodulators enhances tumour-localized immunotherapy. *Nat Nanotechnol* 2018;**13**:746–54.
- Zheng XL, Ge JC, Wu JS, Liu WM, Guo L, Jia QY, et al. Biodegradable hypocrellin derivative nanovesicle as a near-infrared light-driven theranostic for dually photoactive cancer imaging and therapy. *Biomaterials* 2018;**185**:133–41.
- Spicer CD, Jumeaux C, Gupta B, Stevens MM. Peptide and protein nanoparticle conjugates: versatile platforms for biomedical applications. *Chem Soc Rev* 2018;**47**:3574–620.
- Mei YL, Wang RB, Jiang W, Bo Y, Zhang TF, Yu JL, et al. Recent progress in nanomaterials for nucleic acid delivery in cancer immunotherapy. *Biomater Sci* 2019;**7**:2640–51.
- Zheng YL, Ye JX, Li ZY, Chen HJ, Gao Y. Recent progress in sonophotodynamic cancer therapy: from developed new sensitizers to nanotechnology-based efficacy-enhancing strategies. *Acta Pharm Sin B* 2021;**11**:2197–219.
- Li SK, Zou QL, Li YX, Yuan CQ, Xing RR, Yan XH. Smart peptide-based supramolecular photodynamic metallo-nanodrugs designed by multicomponent coordination self-assembly. *J Am Chem Soc* 2018;**140**:10794–802.
- Zhi KK, Wang JC, Zhao HT, Yang X. Self-assembled small molecule natural product gel for drug delivery: a breakthrough in new application of small molecule natural products. *Acta Pharm Sin B* 2020;**10**: 913–27.
- Yang X, Ma C, Chen ZM, Liu J, Liu FY, Xie RB, et al. Single small molecule-assembled nanoparticles mediate efficient oral drug delivery. *Nano Res* 2019;**12**:2468–76.
- Zhi KK, Zhao HT, Yang X, Zhang H, Wang JC, Wang J, et al. Natural product gelators and a general method for obtaining them from organisms. *Nanoscale* 2018;**10**:3639–43.
- Cheng JJ, Fu SY, Qin Z, Han Y, Yang X. Self-assembled natural small molecule diterpene acids with favorable anticancer activity and biosafety for synergistically enhanced antitumor chemotherapy. *J Mater Chem B* 2021;**9**:2674–87.
- Wang JC, Zhao HT, Zhi KK, Yang X. Exploration of the natural active small-molecule drug-loading process and highly efficient synergistic antitumor efficacy. *ACS Appl Mater Interfaces* 2020;**12**:6827–39.
- Cheng JJ, Zhao HT, Yao L, Li Y, Qi BK, Wang J, et al. Simple and multifunctional natural self-assembled sterols with anticancer activity-mediated supramolecular photosensitizers for enhanced antitumor photodynamic therapy. *ACS Appl Mater Interfaces* 2019;**11**: 29498–511.
- Cheng JJ, Zhao HT, Wang JC, Han Y, Yang X. Bioactive natural small molecule-tuned coassembly of photosensitive drugs for highly efficient synergistic and enhanced Type I photochemotherapy. *ACS Appl Mater Interfaces* 2020;**12**:43488–500.
- Wang JC, Zhao HT, Qiao WS, Cheng JJ, Han Y, Yang X. Nano-medicine-cum-carrier by co-assembly of natural small products for synergistic enhanced antitumor with tissues protective actions. *ACS Appl Mater Interfaces* 2020;**12**:42537–50.
- Xi JC, Liu HP. Recent advances in the design of self-delivery amphiphilic drugs and vaccines. *Adv Ther* 2019;**3**:1900107.
- Zhang RS, Qin XF, Kong FD, Chen PW, Pan GJ. Improving cellular uptake of therapeutic entities through interaction with components of cell membrane. *Drug Deliv* 2019;**26**:328–42.
- Pujals S, Giralt E. Proline-rich, amphipathic cell-penetrating peptides. *Adv Drug Deliv Rev* 2008;**60**:473–84.
- Karimi M, Ghasemi A, Sahandi Zangabad P, Rahighi R, Moosavi Basri SM, Mirshekari H, et al. Smart micro/nanoparticles in stimulus-responsive drug/gene delivery systems. *Chem Soc Rev* 2016;**45**: 1457–501.
- Cheng JJ, Li XY, Wang S, Han Y, Zhao HT, Yang X. Carrier-free triterpene prodrugs with glutathione response and biosafety for synergistically enhanced photochemotherapy. *ACS Appl Mater Interfaces* 2021;**13**:245–56.
- Li XS, Lee SY, Yoon J. Supramolecular photosensitizers rejuvenate photodynamic therapy. *Chem Soc Rev* 2018;**47**:1174–88.
- Zou P, Yuan SJ, Yang X, Guo YZ, Li LN, Xu CW, et al. Structural characterization and antitumor effects of chitosan oligosaccharides against orthotopic liver tumor via NF- κ B signaling pathway. *J Funct Foods* 2019;**57**:157–65.
- Zhai XC, Yuan SJ, Yang X, Zou P, Li NL, Li GY, et al. Chitosan oligosaccharides induce apoptosis in human renal carcinoma via reactive-oxygen-species-dependent endoplasmic reticulum stress. *J Agric Food Chem* 2019;**67**:1691–701.
- Deng G, Ma C, Zhao HT, Zhang SQ, Liu J, Liu FY, et al. Anti-edema and antioxidant combination therapy for ischemic stroke via glyburide-loaded betulinic acid nanoparticles. *Theranostics* 2019;**9**: 6991–7002.
- Liu K, Xing RR, Zou QL, Ma GH, Möhwald H, Yan XH. Simple peptide-tuned self-assembly of photosensitizers towards anticancer photodynamic therapy. *Angew Chem Int Ed Engl* 2016;**55**:3036–9.
- Li Y, Lin JY, Wang PY, Luo Q, Lin HR, Zhang Y, et al. Tumor microenvironment responsive shape-reversal self-targeting virus-inspired nanodrug for imaging-guided near-infrared-II photothermal chemotherapy. *ACS Nano* 2019;**13**:12912–28.
- Sawada SI, Sato YT, Kawasaki R, Yasuoka JI, Mizuta R, Sasaki Y, et al. Nanogel hybrid assembly for exosome intracellular delivery: effects on endocytosis and fusion by exosome surface polymer engineering. *Biomater Sci* 2020;**8**:619–30.
- Chou TC. Theoretical basis, experimental design, and computerized simulation of synergism and antagonism in drug combination studies. *Pharmacol Rev* 2006;**58**:621–81.
- Zhao YP, Zhao YN, Ma QS, Sun B, Wang QP, Ding Z, et al. Carrier-free, dual-functional nanorods via self-assembly of pure drug molecules for synergistic chemo-photodynamic therapy. *Int J Nanomed* 2019;**14**:8665–83.
- Ma X, Zhao YL. Biomedical applications of supramolecular systems based on host–guest interactions. *Chem Rev* 2015;**115**:7794–839.
- Qin XH, Zhang MZ, Hu X, Du Q, Zhao ZP, Jiang Y, et al. Nano-engineering of a newly designed chlorin e6 derivative for amplified photodynamic therapy via regulating lactate metabolism. *Nanoscale* 2021;**13**:11953–62.
- Du Q, Qin XH, Zhang MZ, Zhao ZP, Li Q, Ren XM, et al. A mitochondrial-metabolism-regulatable carrier-free nanodrug to amplify the sensitivity of photothermal therapy. *Chem Commun (Camb)* 2021;**57**:8993–6.
- Li XS, Yu S, Lee D, Kim G, Lee B, Cho Y, et al. Facile supramolecular approach to nucleic-acid-driven activatable nanotheranostics that overcome drawbacks of photodynamic therapy. *ACS Nano* 2018;**12**:681–8.
- Gilson RC, Black KC, Lane DD, Achilefu S. Hybrid TiO₂-ruthenium nano-photosensitizer synergistically produces reactive oxygen species in both hypoxic and normoxic conditions. *Angew Chem Int Ed Engl* 2017;**56**:10717–20.
- Xu SD, Yuan YY, Cai XL, Zhang C-J, Hu F, Liang J, et al. Tuning the singlet-triplet energy gap: a unique approach to efficient

- photosensitizers with aggregation-induced emission (AIE) characteristics. *Chem Sci* 2015;**6**:5824–30.
44. Wu WB, Mao D, Xu SD, Kenry, Hu F, Li XQ, et al. Polymerization-enhanced photosensitization. *Chem* 2018;**4**:1937–51.
 45. Kundu PK, Samanta D, Leizrowice R, Margulis B, Zhao H, Börner M, et al. Light-controlled self-assembly of non-photoresponsive nanoparticles. *Nat Chem* 2015;**7**:646–52.
 46. Miyazaki M, Yuba E, Hayashi H, Harada A, Kono K. Hyaluronic acid-based pH-sensitive polymer-modified liposomes for cell-specific intracellular drug delivery systems. *Bioconjug Chem* 2018;**29**:44–55.
 47. Zhang JY, Liu ZN, Lian P, Qian J, Li XW, Wang L, et al. Selective imaging and cancer cell death via pH switchable near-infrared fluorescence and photothermal effects. *Chem Sci* 2016;**7**:5995–6005.
 48. Cheng JJ, Tan GH, Li WT, Zhang HY, Wu XD, Wang ZQ, et al. Facile synthesis of chitosan assisted multifunctional magnetic Fe₃O₄@SiO₂@CS@pyropheophorbide-a fluorescent nanoparticles for photodynamic therapy. *New J Chem* 2016;**40**:8522–34.
 49. Cheng JJ, Wang S, Zhao HT, Liu Y, Yang X. Exploring the self-assembly mechanism and effective synergistic antitumor chemophototherapy of a biodegradable and glutathione responsive ursolic acid prodrug mediated photosensitive nanodrug. *Biomater Sci* 2021;**9**:3762–75.
 50. Yang Y, Xu J, Sun Y, Mo LT, Liu B, Pan XS, et al. Aptamer-based logic computing reaction on living cells to enable non-antibody immune checkpoint blockade therapy. *J Am Chem Soc* 2021;**143**:8391–401.
 51. Kuai R, Yuan WM, Son SJ, Nam J, Xu Y, Fan YC, et al. Elimination of established tumors with nanodisc-based combination chemimmunotherapy. *Sci Adv* 2018;**4**:eaao1736.
 52. Lesniak WG, Chatterjee S, Gabrielson M, Lisok A, Wharram B, Pomper MG, et al. PD-L1 detection in tumors using [(64)Cu]atezolizumab with PET. *Bioconjug Chem* 2016;**27**:2103–10.
 53. Sagiv-Barfi I, Kohrt HEK, Czerwinski DK, Ng PP, Chang BY, Levy R. Therapeutic antitumor immunity by checkpoint blockade is enhanced by ibrutinib, an inhibitor of both BTK and ITK. *Proc Natl Acad Sci U S A* 2015;**112**:E966–72.
 54. Liang C, Chao Y, Yi X, Xu J, Feng LZ, Zhao Q, et al. Nanoparticle-mediated internal radioisotope therapy to locally increase the tumor vasculature permeability for synergistically improved cancer therapies. *Biomaterials* 2019;**197**:368–79.